Out of Thermodynamic Equilibrium Reaction of Zinc-Molybdenum System Monitored by Real-time Rutherford Backscattering Spectrometry

By

AYANDA SOBHOYISE

(3989039)

A thesis

Submitted in fulfilment of the requirements for the degree of

MASTERS OF SCIENCE

In the Department of Physics, Faculty of Natural Sciences,

University of the Western Cape

2021

Supervisor: Dr. L. Kotsedi: iThemba LABS-NRF, Tandetron Laboratory

Co-Supervisors: Dr. N. Mongwaketsi: iThemba LABS, Tandetron Laboratory

Prof. R. Madjoe: UWC, Department of Physics and Astronomy

1

KEYWORDS:

Electron beam evaporation (e-beam)

Zinc

Molybdenum

Bi-layers

Rutherford backscattering spectrometry

X-ray diffraction

Solid phase reaction

Scanning electron microscope

Atomic force microscopy

2

ABSTRACT

Solid phase reaction of bi-metallic thin films of zinc-molybdenum was thermally induced in order to investigate the diffusion kinetics of this bi-metallic system. The Zinc-Molybdenum bi-layers were prepared by depositing a 50 nm thin film of Zinc on a substrate, followed by deposition of 50 nm layer of Molybdenum onto the Zinc film. All this was done in the electron beam evaporation chamber in sequential manner without breaking vacuum. The substrate temperature was at room temperature, the deposition pressure and the power supply current were approximately 1×10^{-6} mbar and 25 mA respectively. The samples were isothermally annealed using in-situ real-time Rutherford backscattering spectrometry using the incident energy of 3.045 MeV. In-situ real-time Rutherford backscattering spectrometry enabled the tracking of atomic diffusion and depth profiling between Zinc and Molybdenum layers while heating the sample. The films were heated from room temperature up to the terminal temperature of 400 °C, at a ramp rate of 3 °C/min. The solid phase reaction between Zinc and Molybdenum started at interphase at approximately 300 °C, the diffusion of Zinc atom and their inter-mixing with Molybdenum continued. As the temperature increases some of the Zinc atoms evaporated of the sample as noted by the decrease width of the Zinc peak. Surface morphology characterization of Zinc-Molybdenum sample at temperatures of interest (300 °C, 340 °C and 380 °C) was performed using scanning electron microscope and atomic force microscope. The micrographs revealed that as the temperature increases the surface roughness evolved as the atoms diffused and mixed. The results also showed at 380 °C a smoother and more continuous film with less cone like structures was formed than as observed at lower temperatures. X-ray diffraction was used to examine crystallinity of the thin films at temperatures 300 °C, 340 °C and 380 °C and at 380 °C, and it showed that a Zinc-Molybdenum alloy was formed as indicated by a Bragg's peak at $2\theta = 41.5$ °.

3

DECLARATION

I declare that "**Out of Thermodynamic Equilibrium Reaction of Zinc-Molybdenum System Monitored by Real-time Rutherford Backscattering Spectrometry**." is my own work. It is being submitted for the Master Degree of Science in the department of Physics in the University of the Western Cape, Cape Town. It has not been submitted before for any degree or examination in any other University.

Signature of candidate……………………….   Date…………………………...

UNIVERSITY *of the*
WESTERN CAPE

ACKNOWLEDGEMENTS

TABLE OF CONTENTS

LIST OF FIGURES

Content   Page

LIST OF TABLES

UNIVERSITY *of the*
WESTERN CAPE

CHAPTER 1: INTRODUCTION

1.1 Background

It is in the best interest of the scientists to understand physical and chemical properties of material based on its proposed application. The physical and chemical properties of the material of interest can be studied by exploring and understanding their thermodynamic nature of the reaction, melting point of the compound used, crystallographic nature of the molecules and growth mechanism of the material, especially in bulk solid state samples in thin film studies [1-2]. The properties of the material of interest can be studied in a solid state, liquid state or gaseous state depending on the type of application. In a liquid state the intermolecular forces of the sample can be studied and quantified. These forces are generally weaker in liquids and as a result, atoms or molecules are able to move relatively easy around each other and are able to take the shape of the container. The study of liquids can be extended to probing the surface tension of the molecules when they come into contact with any surface. Furthermore, the density of liquids and other intensive (colour and boiling point) and extensive (polar and non-polar liquid, cohesion forces) properties can help in understanding liquid samples [3-5].

The gaseous state of matter on the other hand can be studied via their diffusivity, and the intensive and extensive properties can be quantified and expressed using Boyle's and Charles laws. The interaction forces between gas molecules is the weakest but they are able to fill any container because of the weak Van der Waals forces [6-7]. In a solid state, the samples can be prepared as bulk material in a powder form or as thin films on a substrate for a study. The sample can consist of a single element bi-metal, or an alloy consisting of many elements. The interaction and physical properties of these samples can be studied by employing various theoretical model and several characterization techniques [8]. Thin film materials exhibit different properties compared to bulk materials and their physical properties can be exploited for device application in mechanical, thermal and electrical technologies [9-10]. Zinc-Molybdenum (Zn-Mo) alloys have been used in various commercial applications and this led to extensive research of such systems. These systems of alloys have been used as corrosion resistant materials and also in electronic soldering because they are less toxic compared to lead based solders. Zn-Mo systems can be prepared using various deposition techniques including physical and chemical vapour deposition, thermal evaporation, direct current and radio frequency as well as electron beam evaporation which was used in our study to prepare Zn-Mo films. The analysis of Zn-Mo samples prepared using different methods and the results of

13

various characterization techniques have been reported before. However, there is no much literature on preparation of bi-layers of Zn-Mo using electron beam evaporation method and real time RBS analysis is the least used technique for Zn-Mo system. The deposition techniques will be discussed in more detail in chapter 2. Each of the deposition methods has their advantages and limitation depending on the intended application. The application of materials is determined by its properties and these properties can be modified through various processes such as annealing. Materials can be annealed isothermally or non-isothermally and this produces different properties in the material. During the process of annealing in isothermal conditions, heat is spread to neighbouring areas and it crystallises uniformly forming large crystals and thermodynamic equilibrium phases. With isothermal annealing recrystallization is slow and large crystals are likely to be formed [8-12]

In the present study, in-situ real-time RBS was used to isothermally anneal Zn-Mo thin film samples using incident energy of 3.045 MeV. In-situ real-time RBS enables the tracking of inter layer diffusion and depth profiling between Zn and Mo layers while heating the sample. The crystallinity of Zn-Mo thin film at temperatures of interest and the morphological properties were investigated.

1.2. Aim of the study

The aim of this study is to prepare thin films of Zn-Mo on substrates using electron beam evaporation system (e-beam), compare and track inter-layer diffusion kinetics using real-time Rutherford backscattering spectrometry (RBS).

1.3. Significance of study

- o Getting more knowledge and experience on the synthesis of thin metallic films using different preparation methods
- o Acquire significant knowledge on different characterisation techniques and their applications and also how radiation interacts with matter during different processes.

1.4 Thesis layout

Chapter 1: Introduces and provides the aim and the significance of the study.

Chapter 2: A literature overview of the Zn-Mo bi-metallic and related systems and the effect of thermal annealing on the properties of metallic thin film materials. The chapter also covers

various studies conducted on Zn-Mo thin metallic alloy prepared using different techniques. It also discusses the vacancy and interstitial diffusion in metals.

Chapter 3: The chapter covers experimental methods for sample preparation and characterisation techniques used. This chapter also details the processing technique and the procedures involved in fabricating Zn-Mo thin films.

Chapter 4: Presentation and discussions of results from all characterisation techniques.

Chapter 5: This chapter summarizes conclusions drawn from this work and provides recommendations for possible future work.

CHAPTER 2: LITERATURE RIVIEW

2. INTRODUCTION

The most interesting way to study bimetallic systems is in the area of soldering. Soldering is a method of binding multiple things together by melting and inserting a filler metal with a lower melting point than the adjoining metal into the joint. This approach arises from the drive to find cheap and non-hazardous replacements of lead (Pb) based solders for high temperature applications. Several alloys systems are currently being researched with Zn based alloys showing most promising potential. Zn based alloys are also applicable in high temperature soldering even though they have drawbacks. Zn has relatively low galvanic potential and it can corrode at a very slow rate. This metal has poor wetting behaviour due to oxygen affinity. However, the lifespan and reliability of a material depend on the continuous variation of surrounding processes which are capable of causing damage and corrosion. Zn based alloys have been widely used in the field of material science, and there is still more research being carried out to exploit the physical properties of these alloys. Low melting point and relatively low reactivity of Zn is well suited for vast alloying with wide range of metals. Pure Zn coatings have been widely used as a sacrificial coating to protect steel structures from corrosion. Zn based coatings with the addition of Mo dispersed consistently over the layer are used to improve corrosion. Chromate conversion layers have been widely applied to increase corrosion resistance but because of their genotoxic effects, Mo has since been seen as a potential replacement. Mo is considerably much less toxic and favourable to be an alternative to chromate films on Zn, which are widely used to intensify corrosion resistance of Zn based layers. The addition of Mo to Zn based layers has proved to have a great effect on the corrosion behaviour of Zn and Zn alloys, and it is widely known that it improves abrasion hardness, toughness and corrosion resistance of alloys. Zn-Mo thin films can be prepared using chemical and physical vapour deposition techniques such as DC sputtering, spray pyrolysis, pulsed laser deposition and electron beam evaporation system. Spray pyrolysis has been considered as the most effective tool to prepare different kinds of thin films which include nanophase materials. This technique is considerably predominant compared to others since it can be adapted easily for production of extensive area films and has excellent control of chemical uniformity in multi-component system [45-51].

2.1. Deposition techniques

2.1.1. Physical vapour deposition

Physical vapour deposition (PVD) is a coating technique that involves the transfer of material by removing atoms from a target material to a substrate. This process can be facilitated by using stimuli such as energetic electrons emitted by an electron gun, resistively heated host boats and ionized gas particles. These stimuli generally interact with the target material resulting in either melting, evaporation of the material direction sublimation of the atoms or just direct sputtering off of atoms due to bombardment. These PVD technologies cover a vast range of deposition techniques including electron-beam evaporation, thermal evaporation and reactive direct current (DC) and radio frequency sputtering. During deposition of the thin films, the gaseous state vapour from the target material condenses onto a substrate resulting into a solid phase thin film [23-25]. The four steps involved in the process of PVD are illustrated in Fig. 2.1. below. The first step is the evaporation of the material to be deposited using a high-energy source such as an electron beam or ions which evaporates atoms from the surface. The second step is the transport of the vapour to the substrate to be coated. This step is followed by reaction between the metal atoms and the appropriate reactive gas (such as oxygen, nitrogen, or methane) during the transport stage, and lastly the deposition of the coating.
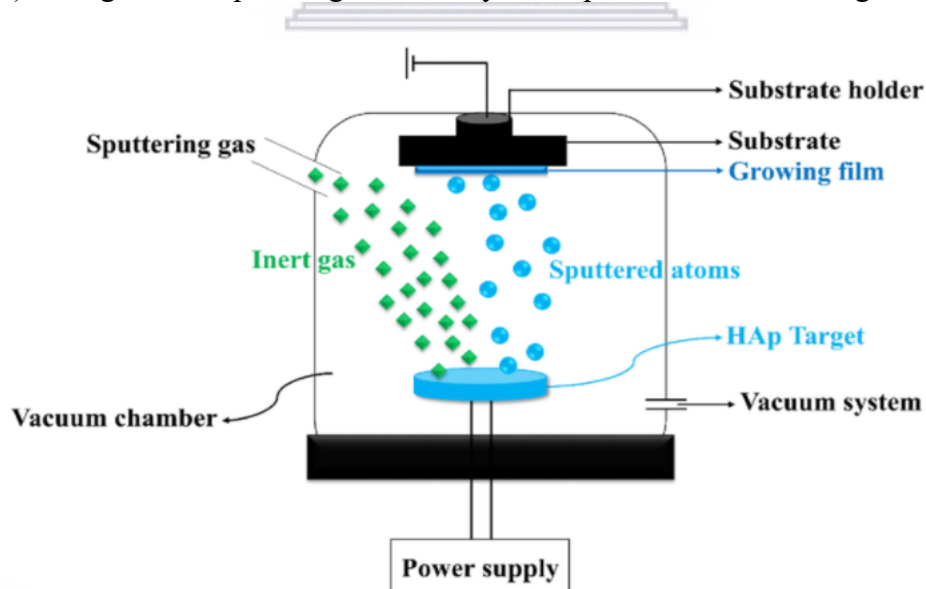
Fig. 2.1. *Schematic diagram showing steps involved in the process of PVD [24].*

2.1.2. Thermal evaporation

Thermal evaporation is a thin film deposition method which uses vacuum technology for applying coatings of pure materials to substrate surfaces. This method involves heating of material in a high vacuum chamber. This deposition techniques generally need good vacuum chamber, a thick bell jar or metal chamber which is evacuated using a rotary pump followed by a turbo pump. This is done to remove any air or moisture in the chamber which might contaminate the samples. When a good base pressure is reached, an evaporation boat (usually Tungsten and Molybdenum) loaded with a material to be evaporated is subjected to heating. The boat is resistively heated by applying a high potential difference at its ends. Applying high potential difference causes the particles of the heated solid material to be released through evaporation. At the end of this process a thin film will be deposited on a substrate [26-27]. Fig. 2.2 shows a typical experimental set up of a thermal evaporator.
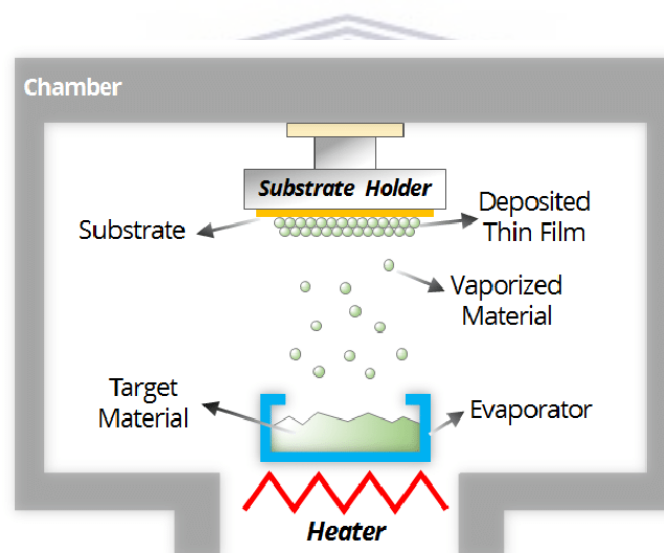
Fig. 2.2. *A typical experimental setup of a thermal evaporator [37]*

2.1.3. Electron beam evaporation

Electron beam evaporation is a physical vapour deposition technique, where an electron beam is produced from a resistively heated tungsten filament electron gun (through thermionic process), which is controlled by high voltage source. The thermionic electron beam is guided by the electron spray shield and the bending magnet which strikes the target material placed in a water-cooled crucible. Thermionic electrons are released or produced when a high potential difference is applied at the ends of a tungsten filament. These electrons are then directed to a

water-cooled crucible containing the target material. A spray shield and a magnet are used to adjust the position of the electrons onto the target. When the electrons heat the target material this result in melting and evaporation of the material or sublimation. All the depositions are conducted in a high vacuum pressure environment and a crystal monitor is used measure the deposition rate and thickness of the grown film. [28-29]. Fig. 2.3 shows a schematic representation of the electron beam evaporation system.
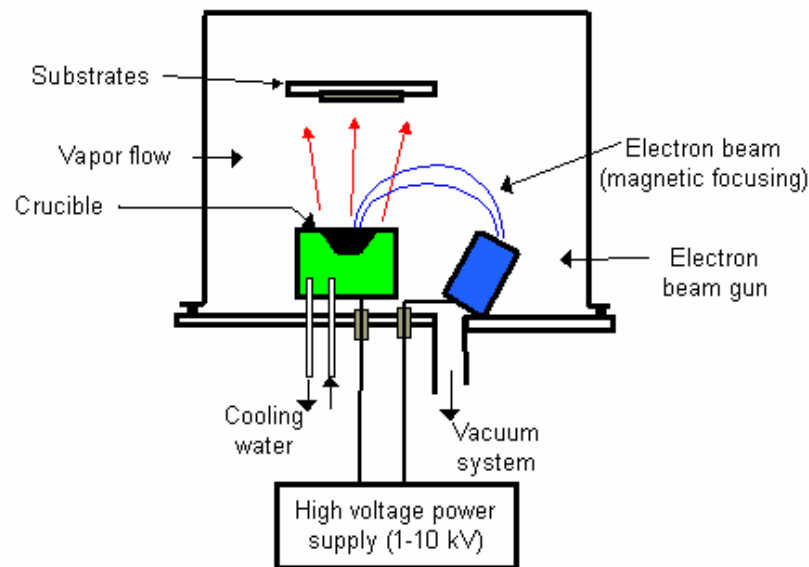
Fig. 2.3. *Schematic representation of the electron beam deposition system* [38]

2.1.4. Direct current and radio frequency sputtering

Sputtering is a process in which small particles of a solid material are ejected off its surface after being hit by intense plasma or gas particles. It can be an undesirable source of wear in precision components because it occurs naturally in space. Direct current (DC) and radio frequency (RF) are the two modes of sputtering that are generally used. The RF mode is used for the deposition of the dielectric materials while the DC mode is used to deposit metals. The argon atoms that are ionized by a DC or RF source are focused toward the surface of the target material to be deposited. The ionized argon atoms sputters atoms off of the target resulting in metal vapour that is transferred directly toward the substrate and grow according to the deposition conditions. The substrate temperature, pressure and the flow rate of the argon gas from the cylinder can be controlled electronically [30-32]. Fig. 2.4 shows a typical experimental setup of a sputtering chamber.

19
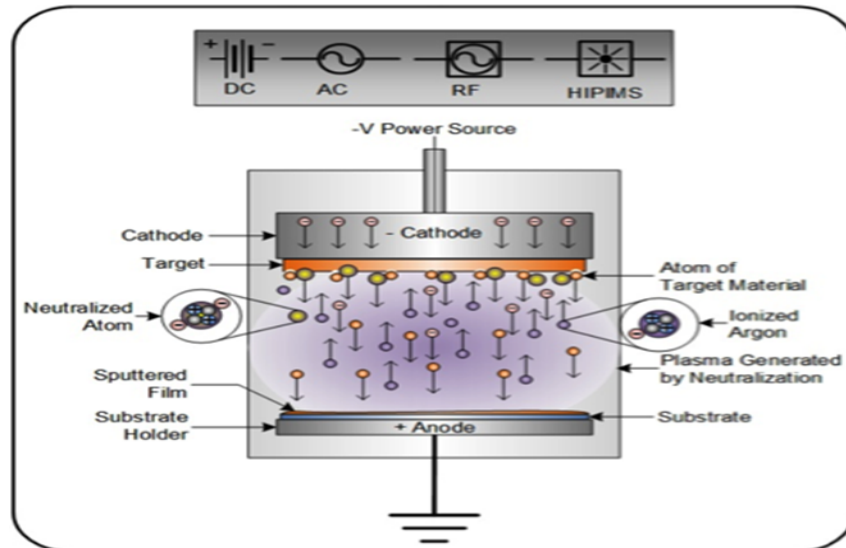
Fig. 2.4. *A typical chamber of an RD and DC sputtering deposition equipment [39]*

2.1.5. Chemical vapour deposition

Chemical vapour deposition (CVD) is a coating method that utilises chemical reactions which are thermally controlled at the surface of heated substrate with gaseous reagents. These reactions may additionally contain the substrate material itself however they frequently do not. CVD is a technique that is used for producing solid thin films and coatings using chemical reactions. These reactions are thermally controlled at the surface of heated substrate with gaseous reagents. CVD involves flowing a precursor gas or gases into a chamber containing one or more of the heated objects to be coated. Chemical reactions occur on and near the hot surfaces, resulting in the deposition of a thin film on the surface. In this method, the precursor is heated into a gas form at an excessive temperature and is then deposited on the surface of the substrate because of response with the recent surface and thus forms a thin-film layer on the surface. This technology is broadly employed in producing bulk substances and powders with good purity, deposition of materials surface, and development of composite material through infiltration methods. The CVD process can be categorised as low-pressure CVD (LPCVD) and atmospheric-pressure CVD (APCVD).LPCVD is a chemical vapour deposition technology that uses warmth to initiate a reaction of a precursor gas on the solid substrate resulting in the formation of solid phase material onto the target surface. [33-35]. Fig. 2.5 displays low pressure CVD processes.
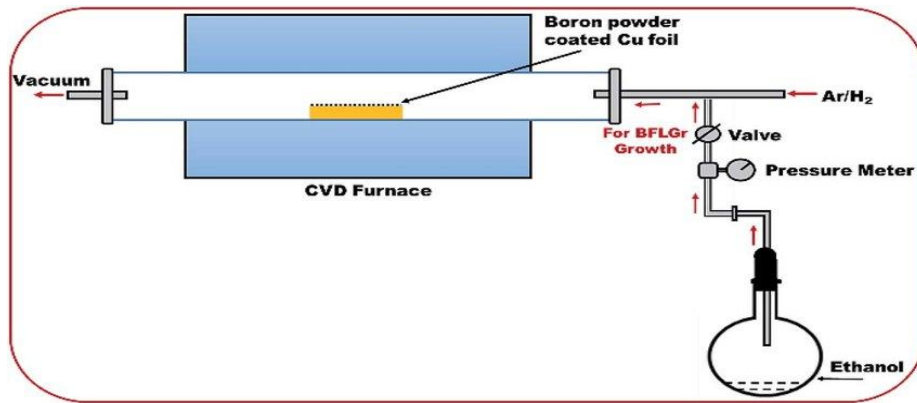
Fig. 2.5. *Representation of low-pressure CVD (LPCVD)* [112].

APCVD is a CVD method which is used for deposition of doped and un-doped oxides at atmospheric pressure. The deposited oxide has a low density and the coverage is moderate due to a relatively low temperature. The substrate is exposed to volatile precursors at atmospheric pressure followed by a reaction or decomposition on the surface to form a deposit [35,42]. Fig. 2.6 shows diagram representing atmospheric-pressure APCVD method.
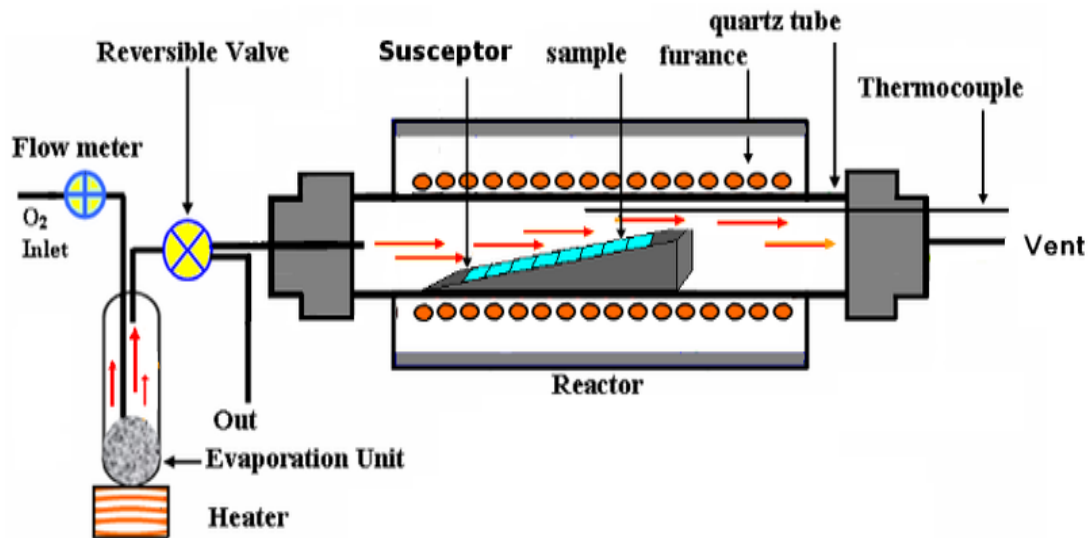
Fig. 2.6. *Schematic representation of atmospheric-pressure CVD (APCVD)* [113]

Our study focuses on reaction dynamics of Zn-Mo system prepared using electron beam evaporation system which is further explained in chapter 3. This technique is advantageous when comparing to other techniques with regards to independence and freedom in control of effective microstructure and composition. Manipulation of crucial parameters such as substrate

temperature, evaporant composition, and thickness are easily managed through electron beam evaporation system accessories.

2.2. Thin Film Growth

A general process that takes place when a film grows on substrate can be described in four stages; *(i)* atoms adsorption on the substrate where atoms or molecules find an energetically favourable side on the substrate and become absorbed. This is followed by *(ii)* surface diffusion, where the atoms or molecules diffuse on the surface of the substrate and interacts with other atoms. This then leads to *(iii)* nucleation stage where more atoms or molecules bond together and start to grow. The final stage is *(iv)* coalescence of the nucleation from all sides resulting in thin film growth [13-15]. A general schematic representation of thin film growth on substrate is illustrated in Fig. 2.7 below.
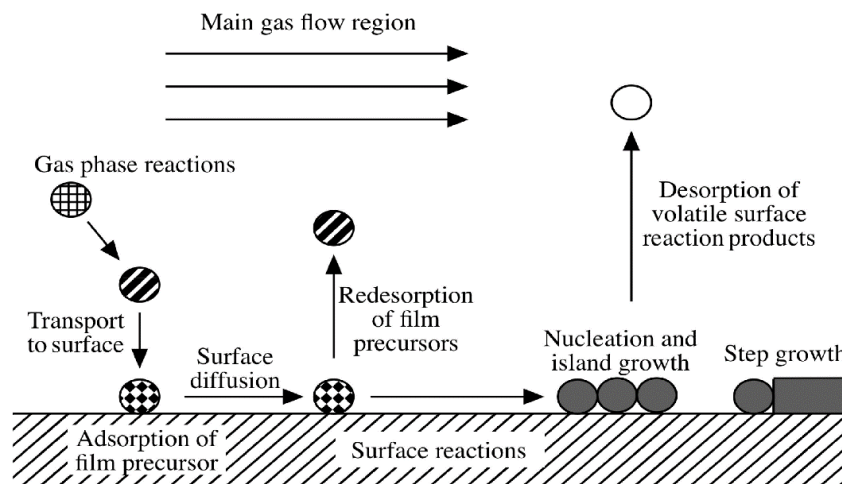
Fig. 2.7. *A general schematic representation of thin film growth on a substrate* [2]

The film grown on substrate can turn out to be a smooth continuous film, rough or a film with an under-layer that is continuous with islands of molecules on top. This feature of thin film is related to a specific growth mechanism that the film was subjected to. The three generally accepted growth mechanism that a thin film growth can follow are the Volmer-Weber (V-W), Frank Vander Merwe (F-M) and Stanski-Krastanov (S-K) [16-17].

In the V-W growth mechanism the prominent feature of the thin film is usually a rough surface with cluster of islands or cracks that are visible on the film. This is due to the atoms to atoms forces being stringer than the atom to substrate force [18]. In the S-K growth mechanism, the first few layers tend to be continuous because the sum of the free energy associated with the free surface energy of the free surface (in this case the film) and the interface between the

22

substrate and the film is relatively equal or less to the free energy associated with substrate surface. This scenario leads to thermodynamically stable systems in the first few layers. As the film grow this reverses and the film gets into an unstable thermodynamic circumstance, which leads to islands formation onto a uniform film [19-21]. The mostly preferred thin film growth mechanism is the F-M where the grown films are smooth and continuous and have a layer by layer type of growth. In this mode the overall free energy decreases faster in the first few layers of the film before stabilizing down to a constant gradual decrease in free energy. Fig. 2.8 shows a graphical representation of the three growth mechanisms [22].
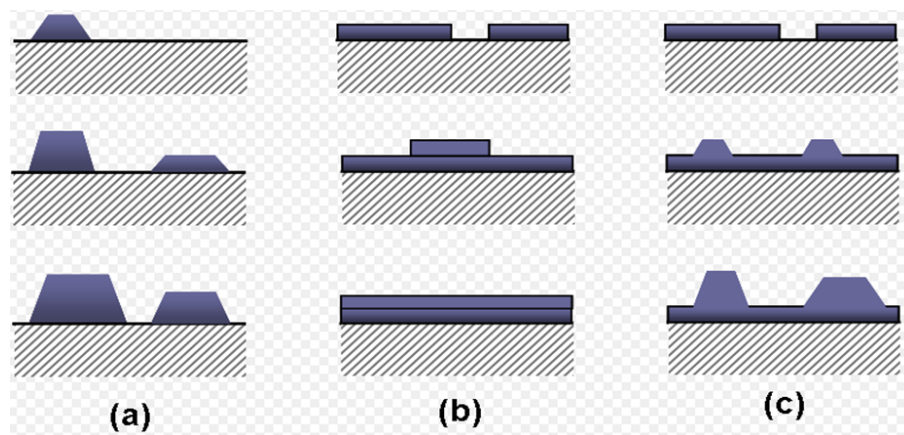
Fig. 2.8. *Cross-section views of the three primary modes of thin-film growth including (a) Volmer–Weber (VW: island formation), (b) Frank–van der Merwe (FM: layer-by-layer), and (c) Stranski–Krastanov (SK: layer-plus-island) [36]*

2.3. Nucleation and growth kinetics in solids

When material is annealed its atoms are randomly activated and are moving from one position to another, thus self-organising and forming new structures. Nucleation is the formation of a new thermodynamic phase which provides the scope on how long for a newly formed phase to be visible, see Fig. 2.9 below. Population density of newly formed crystals and the rate at which are formed is needed to determine the nucleation rate [102-103].

23
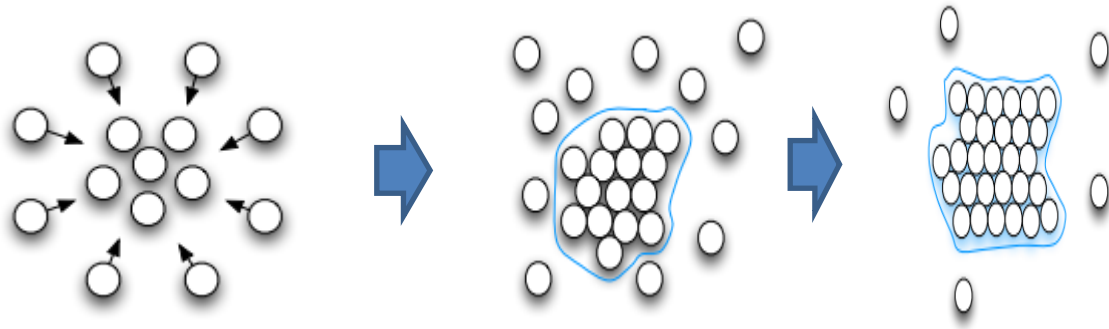
Fig. 2.9. Diagram showing how atoms combine to form a new thermodynamic phase.

Nucleation in solids and in semi-conductors plays a vital role which includes modification of mechanical properties (e.g. ductility). When new phase is formed from two pure materials, new interfaces are also created, leading to the increase in interfacial energy and the driving force behind is Gibb's energy (G). Fig. 2.10 shows the free of the nucleus as a function of its radius displaying surface and volume contributions. The decrease in free energy by combination of two pure materials to form new phase results in an energy gain according to the shown figure [104-105].
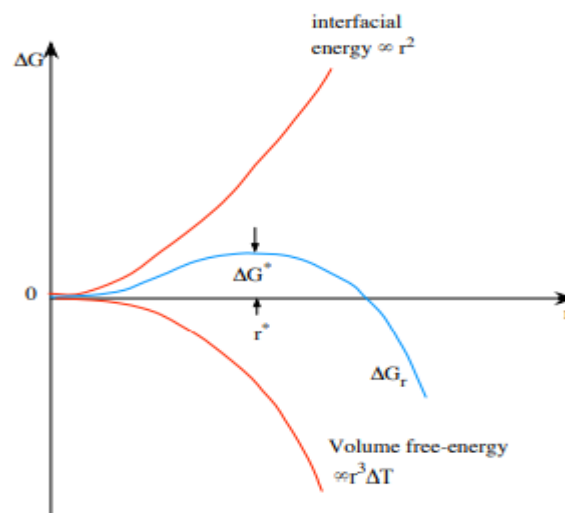
Fig. 2.10. Representation showing free energy of nucleus as function of its radius which shows the surface and volume contributions [104].

24

2.4. Diffusion mechanism in metals

Diffusion is the movement of atoms or molecules from an area of high concentration to a region of low concentration and can take region in gases, liquids, or solids. In solids, diffusion occurs due to thermally-activated random movement of atoms until the material is at absolute zero temperature and individual atoms maintain vibrating and subsequently move within the material. In metals, the two dominating types of diffusion mechanisms are the vacancy diffusion and interstitial diffusion [110].

2.4.1. Vacancy diffusion

In vacancy diffusion mechanism, the diffusing particles migrate from one point void to the next using rapid, seemingly random jumping. The availability of point vacancies throughout the crystal lattice is required for vacancy diffusion to take place. The movement of atom into a vacant site corresponds to the movement of vacancy in the opposite direction. With increasing temperature the charge of crystal stable state diffusion increases as shown in Fig. 2.11 [96,98].
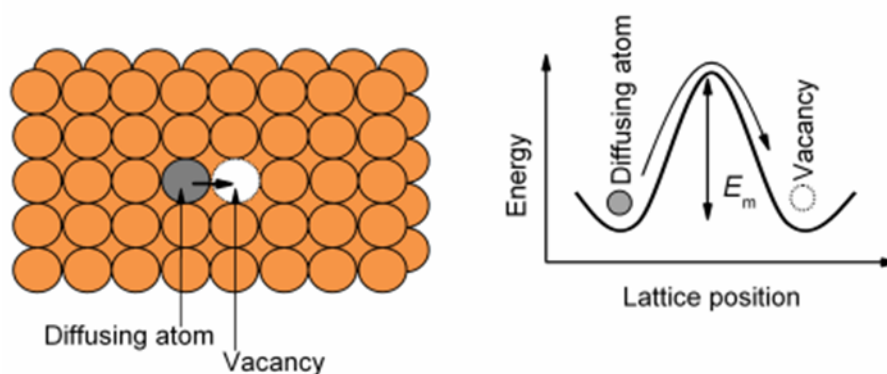
Fig. 2.11. *Diagram of vacancy diffusion showing atoms moving to available vacancies.*

The movement of atom into a vacant site corresponds to the movement of vacancy in the opposite direction. This diffusion mechanism is characteristic of impurity atoms that have comparable atomic measurement as the matrix atoms. In figure 6 particles jump from one point vacancy to the next at a quick, virtually random rate and the rate of crystal solid state diffusion increases with temperature [96,98,117].

2.4.2. Interstitial diffusion

Interstitial diffusion is the movement of an interstitial impurity from one interstitial site to any other interstitial site and is a characteristic of small atom impurities. This diffusion is usually

quicker than vacancy diffusion due to the fact that bonding of interstitials to the surrounding atoms is normally weaker and there are many extra interstitial sites than vacancy sites to jump to and the direction of flow of atoms is opposite the vacancy flow direction as shown in Fig. 2.12 and in the current study interstitial diffusion is applicable [96,97,99].
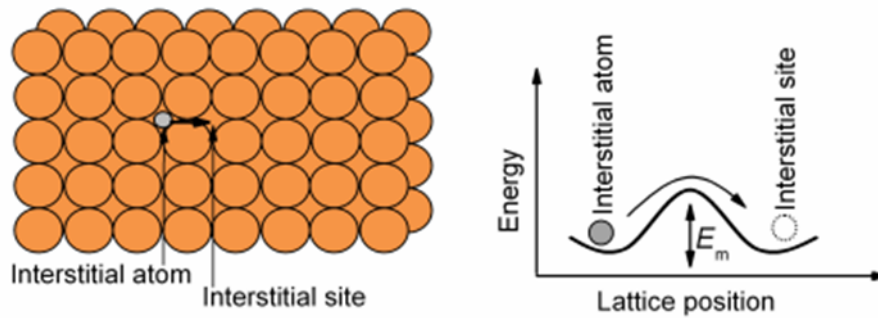
Fig. 2.12. *Schematic representation showing interstitial diffusion.*

In Fig. 2.12 a smaller atom on an interstitial site diffuses through the lattice between host atoms. With this method, there is still an energy barrier to overcome, but it is lower due to the smaller atom, and there are also many vacant places for it to disperse to [118].

2.5. Zinc-Molybdenum Thin Films

Zn-Mo systems have found applications in various spheres of every day technological applications and this has led to more research being conducted on these systems. Previous studies focused on factors affecting crystalline size of both Zn and Mo films, atom mixing and phase formation. In a study by Hara et. al. (2020) a solution of citrate complexes and mixed Zn (I)-Mo (VI)-citrate was used to grow films. It was reported that in preparing the films, the reduction process was related to zinc citrate and Zn (I)-Mo (VI)-citrate mixture. The influence of chemical additives (Triton, D-sorbitol and PEG-2000) on the quality of the films was investigated to see its effect on the morphology of microstructures. The XRD results revealed that a hexagonal closed packed structure was dominant in a solution with PEG-2000, while a solution with D-sorbitol and Triton exhibited hexagonal closed structure Mo-Zn with MoO_2 phase present. The physical properties of the Zn-Mo alloy were studied in order to obtain its melting point profile under nitrogen ambient. Differential thermal analysis (DTA) was a characterization technique of choice for this study of melting temperature profile. The results of this study indicated that Zn-Mo have a melting temperature of approximately 416 °C and

26

XRD results revealed that the grain size of the Zn-Mo alloy decreased with increasing Mo content and no intermetallic phases were formed [48].

Zn-Mo thin films were also prepared and reported by Olvera et al. (2017) where a mechanical process used was mill-balling of Zn and Mo down to a crystal size of approximately 36 nm. The starting martials were 50 Mo + 50 Zn (wt %) powders. The ball milling process was done in ambient conditions using high energy planetary pulverisette for 100 hours. The microstructure of the sample was studied using XRD and the measurements were done for different milling times as shown in Fig. 2.13 [108].
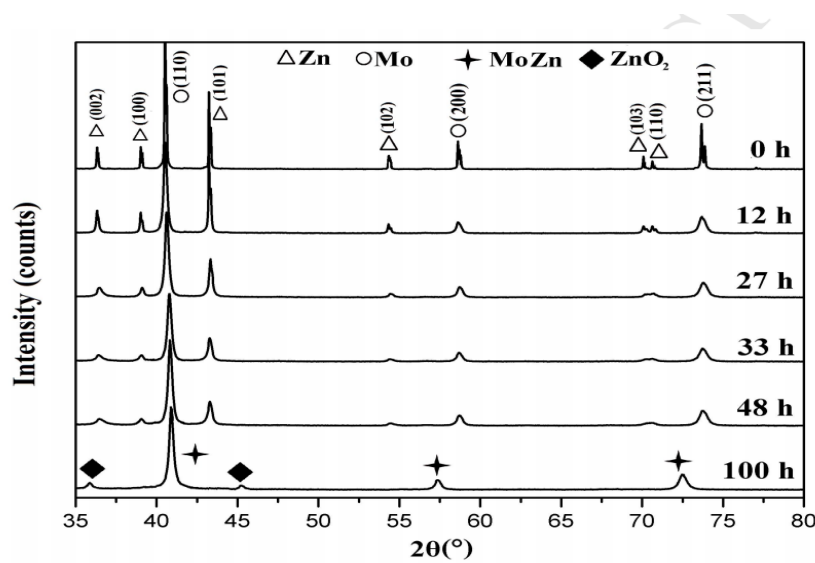
Fig. 2.13. *The X-ray diffraction patterns of the Zn-Mo for different milling times [108].*

The XRD results showed that at 0 hours milling sharp Bragg peaks of Mo and Zn were observed with Mo and Zn exhibiting body centred cubic and hexagonal phase respectively. When the milling duration was increased step-wise, Mo diffraction peak shifted due to dissolution of Zn into Mo matrix. At longer milling times there was larger shit of Mo diffraction peaks accompanied by diminishing Zn diffraction peaks. This led to a formation of Mo-Zn intermetallic phase with a body cubic centre. The formation of Zn-Mo intermetallic phase was only possible since due to mechanical alloying technique used being non-equilibrium synthesis technique. The decrease in the crystalline size also contributed to the Zn-Mo formation due to the diffusion length and increased surface area [108].

Brewer et. al. (1980) and Landolt-Bornstein et al. (2008) proposed the theoretical Zn-Mo equilibrium phase diagram. The diagram in Fig. 2.14 shows formation of two intermetallic phases of $MoZn_7$ and $MoZn_{22}$. The (Mo) + ($MoZn_7$) two-phase region is located at $\leq$ 88.4 at %

27

Zn, and the MoZn$_{22}$-rich phase can only be found at $96.4 \leq$ at % Zn ≤ 97.1. This MoZn$_{22}$-rich phase does not exist in the ≥ 97.1 at % Zn region [106,107].
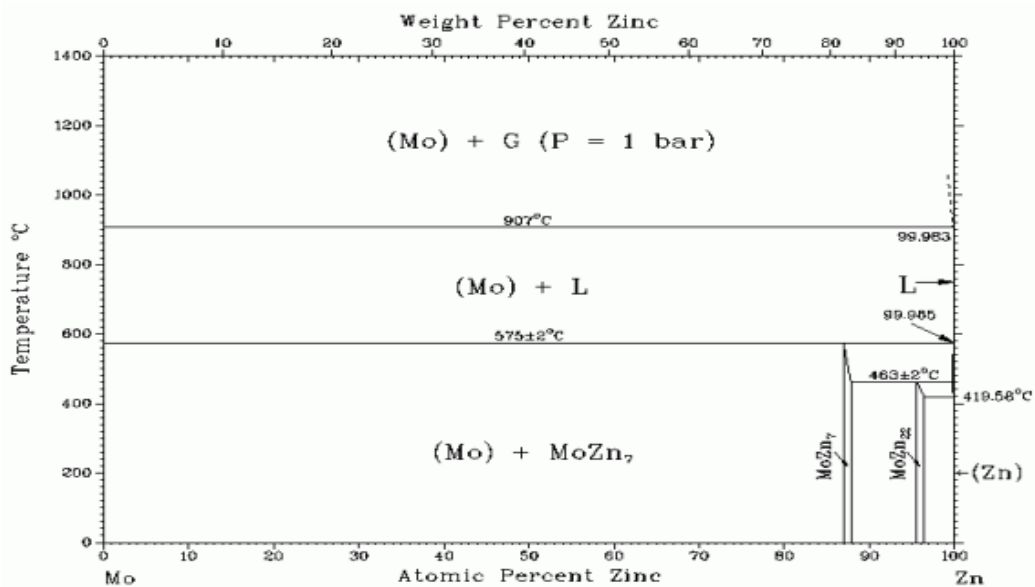
Fig. 2.14. *Mo-Zn equilibrium phase diagram* [106,107]

Zn-Mo layers electrodeposited from the aqueous citrate solution were studied. Aqueous citrate solutions were proposed as baths for electro deposition of Zn–Mo alloy coatings because are non-toxic and form strong complexes with Zn and Mo. The results showed that the surface morphology of Zn–Mo coatings differs according to the Mo content and the substrate used also influenced the morphology of Zn–Mo coatings. XRD analysis did not show the presence of Mo oxides, neither metallic Mo nor other Mo compounds. Only the hexagonal system of the Zn phase was present in the deposits found [47,49].

Kosugi et al. (2017) studied effect of the addition of Mo on the structure and corrosion resistance of Zinc–Iron (Zn-Fe) plating. The preparation of Zn–Fe–Mo plating was performed by considering different pH values of the range 4.0 to 5.7. 10 mA cm^{-2} while the current density was fixed. The intense peaks of Zn-Fe-Mo alloy phases were detected as the Mo concentration decreased as shown in Fig. 15 below. The addition of Mo into Zn–Fe was considered to improve its corrosion resistance. The plating obtained by this experiment showed high corrosion resistance when the electrically-deposited layer formed a Fe$_3$Mo-based alloy phase [9].
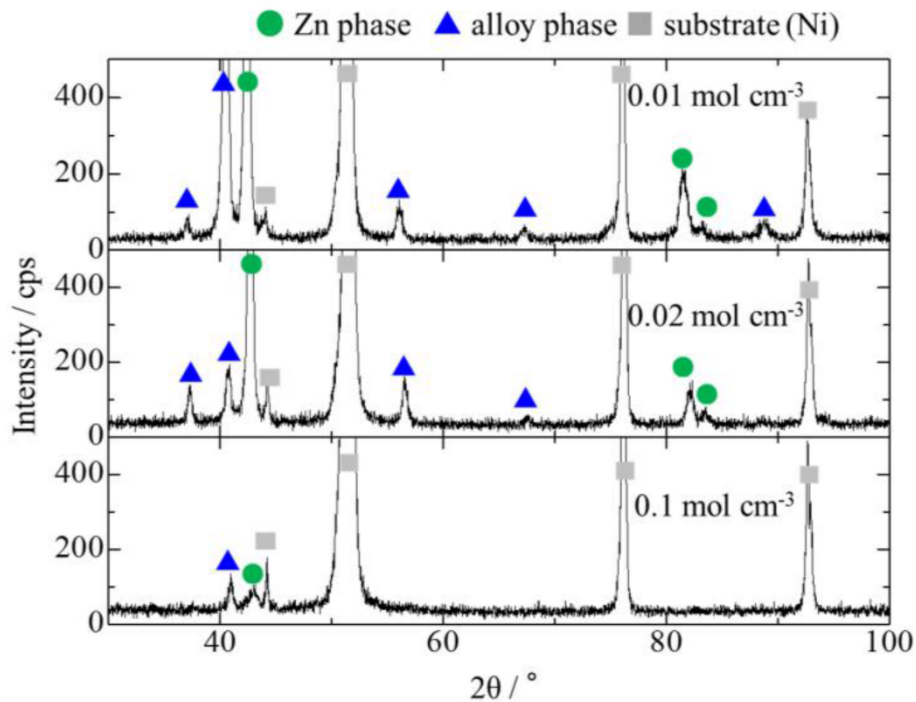
Fig. 2.15. *XRD patterns of the Zn–Fe–Mo plating deposited from a plating bath with different Mo concentrations [9].*

Świątek et al. (2017) examined structural and microstructural properties of Zn-Mo alloy layers electrodeposited from aqueous citrate solution. The surface morphology of Zn-Mo coatings differed according to the content of molybdenum. Mo content was characterized by flake-like particles protruding from the compact cellular-platelet layer. The layers with high Mo content additionally consisted of agglomerates of short needles and elongated platelets. XRD was used to further characterise the Zn-Mo layers and single-phase deposits with the same type of crystal lattice (hexagonal) were visible on the XRD patterns of Zn-Mo layers. With the increase in the content of Mo atoms in the Zn structure it was also observed that the shape of the crystallite varied from flattened oval to almost spherical and then tended to plate shape. The presence of ZnO was also detected in the layer comprising of the highest number of Mo atoms [119].

Another study on Zn-Mo layers demonstrated that the surface morphology of Zn-Mo coatings differed according to the Mo content and the substrate used have an influence on the morphology of Zn-Mo coatings. XRD data indicated that the presence of Mo causes fragmentation of the crystallites and that the increase in the content of Mo atoms in the Zn structure, the crystallite volume drops sharply and then reach an almost constant value with the shape of the crystallite also slightly altered [47].

29

2.6. Lead Free Zn Alloys

In a long list of Pb free alloys that have been researched to replace Sn-Pb, Zn alloys have been proposed as a candidate in the area of high temperature solders. Various metals have been tried for alloying Zn to form solders and several research groups have worked on Zn-Sn [41]. Kim et al. (2008) reported on Zn-xSn system (with x = 20, 30, and 40 wt %) and it was noted that all the samples composition showed good electrical and thermal conductivity and no inter-metallic compound formation. Other alloys that were studied (such as Au-Sn and Bi-Ag) as substitutes for Pb free, appeared to be brittle when inter-metallic compound was formed and this led to poor performance as high temperature solders [41,55].
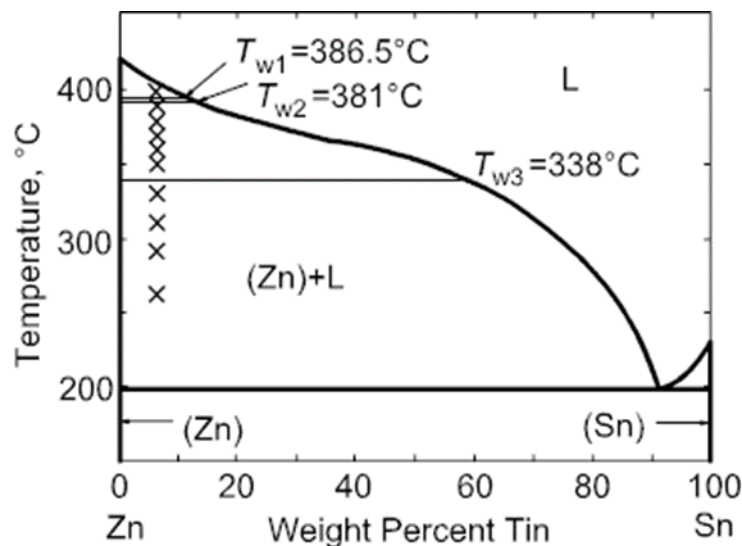
Fig. 2.16: *Zn-Sn binary phase diagram at standard temperature and pressure [55].*

Fig. 2.16 shows a phase diagram of Zn-Sn and from the diagram there is no evidence of the existence of inter-metallic phase. One of the drawbacks of Sn-Zn system as a high temperature solder is its eutectic temperature of approximately 200 °C. At temperatures of around 250 °C, a solid liquid transformation takes place and this is difficult to control due to expansion of the liquid. Several cures to this phenomenon have been explored and this includes restricting Sn wt % loading to below 30 %. This result in approximately less Zn-Sn liquid at eutectic temperature, with an effect of relative stability and control of the solders at high temperature. Nevertheless, more work is needed to be done in this system [55,56].

Aluminium (Al) is the other element that have been used to alloy Zn for soldering purposes. Agapie et al. (2015) reported that the most promising Zn-Al composition for soldering is from the binary phase diagram with eutectic Zn-5-6 wt %-Al alloy [57]. The samples in this study were prepared by melting the metals in an electric graphite crucible bars as electrical resistors under flux blanket. The resultant molten alloy was cast in a mould to obtain bar. Similarly to Zn-Sn system, Zn-Al alloy exhibited no inter-metallic crystallographic phase as observed from binary phase diagram in Fig. 2.17.
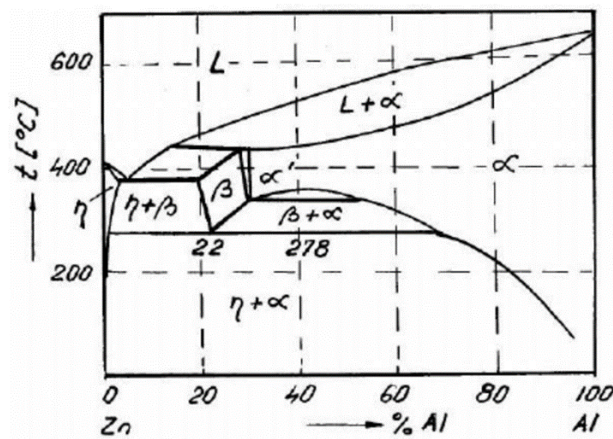
Fig. 2.17. *Zn-Al binary thermal equilibrium phase diagram* [57].

Based on the phase diagram data, the eutectic Zn-0.8-Al-3 wt % has the most promising physical properties for high temperature soldering, due to its melting point of approximately 380 ℃. By increasing the Al content, it has been observed that the conductivity of the Zn alloy increases. The Zn-Al system with 0.83% wt % Al loading has the most promising physical properties for high temperature soldering due to its melting point of approximately 380 ℃. By increasing the Al loading it has been observed that the conductivity of the Zn alloy also increases [57].

Zinc-Nickel (Zn-Ni) have also been investigated to improve the wettability of the zinc alloys for soldering. Mallick et.al. (2016) prepared samples from high purity micro-powders of Ni and Zn blocks. Ni powder was pre-heated and added to a Zn melt prepared in a graphite crucible heated by gas fired pit furnace. The melt was homogenised by manual stirring with a desired proportion of Ni added in the melt. They have found that increasing Ni content has had an advantageous effect on the Zn-Ni solder alloy. The alloying contents increased hardness and

31

tensile strength with the formation of Zn–Ni intermetallic [58]. Fig. 2.18 below is an XRD spectrum showing Zn phase and gamma phase of Zn-1.5 wt %-Ni alloy.
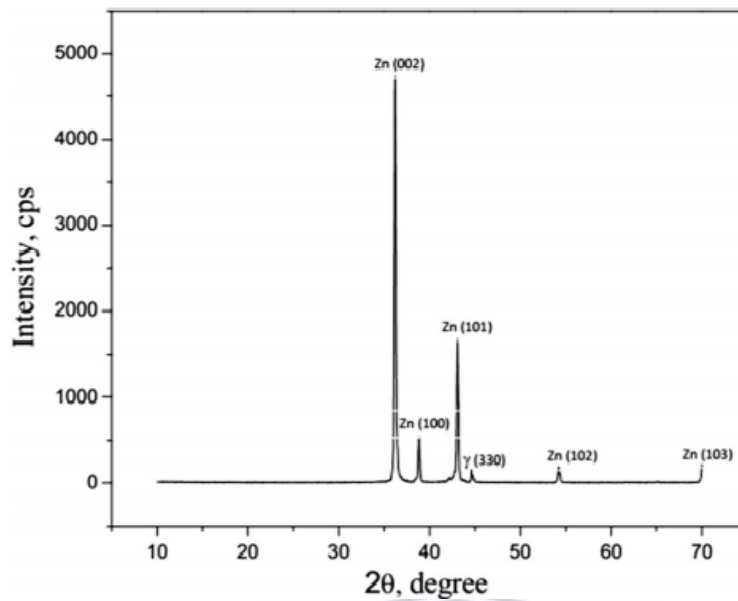
Fig. 2.18. *X-ray diffraction patterns of Zn-Ni alloy* [58].

The XRD patterns of the existence of an intermetallic compound is observable at diffraction angle of approximately $2\theta = 44.5°$. This observation of the intermetallic compound is consistent with the absence of a Ni peak diffraction peak. The phase diagram of the system as shown in Fig. 2.19 displays all the possible stoichiometric phases that can be realised from this system [58].

Binary Zn-Mg alloy has also been studied for soldering application and such system is mainly for light alloy uses. Zn-Mg has the ability to improve the mechanical and electrical of Zn for better soldering. A series of Zn-Mg alloys with varying Mg wt % were prepared by Galib et al. (2019). The XRD patterns of the Zn-Mg alloys in Fig 2.19 shows (a) show formation of intermetallic phase Zn_2Mg_{11} at approximately 43° angle. This phase is also illustrated in the phase diagram of the system on Fig. 2.19 (b).
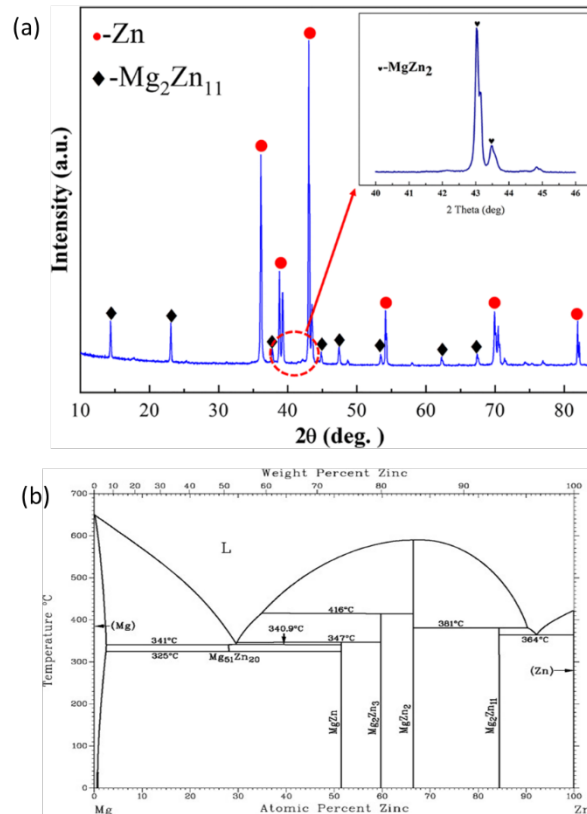
Fig. 2.19. *(a) The X-ray diffraction patterns of Zn and Zn-Mg, (b) phase diagram of Zn-Mg system [109].*

2.7. Annealing

Annealing is a heat treatment that affects the properties of materials and it improves ductility and the strength of the metallic system. The process of annealing affects the surface morphologies of materials and their physical, chemical, optical and catalytic properties [51]. When a material undergoes annealing, its atoms are activated thermally and this leads to structural changes as the temperature increases. During annealing, atoms in the material become more energetic and thus increases the rate of diffusion. Diffusion can be activated annealing by laser heating and thermal annealing [96,97]. The movement of atoms and variations in the structure during the process of annealing is represented in stages namely; recovery, recrystallization and grain growth as shown in Fig. 2.20.

33
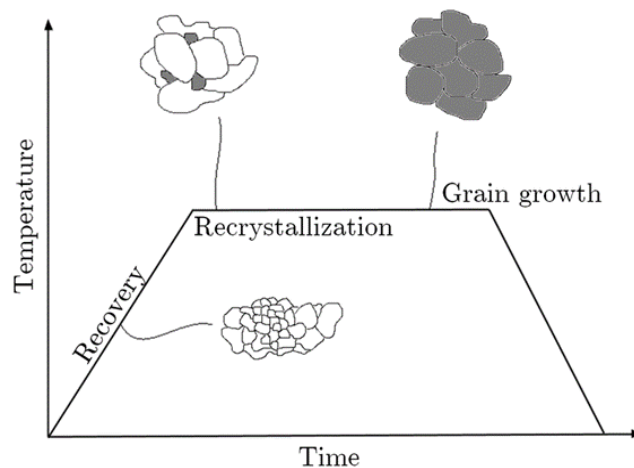
Fig. 2.20. *Schematic representation of the three stages of annealing [111].*

The recovery stage occurs before the strain free grains may appear at very low temperatures of the annealing process. At this stage the material is softened and defects such as dislocations are minimized and the internal stress is removed. The second stage is recrystallization where the newly appeared strain free grains combine to replace the deformed ones by internal stress. During grain growth stage, the microstructure roughens to form structure different from the original before the process of annealing [100,101,111].

2.7.1. Real-time RBS annealing

Real time RBS is the most convenient way to carefully monitor the growth kinetics in bi-metallic systems through ramped isothermal temperature annealing. This is an accurate and powerful technique to study solid state thin film reactions. With real time RBS one can study all the phases of the system from generated spectra throughout in a single experimental run using one sample. This approach is referred to as real-time RBS due to the fact the data from the measurement is generated in real-time through the annealing. The advantage of real-time RBS over other in-situ strategies such as XRD and resistance measurements is that the thickness of the growing layer can be measured as function of temperature. Real-time RBS provides excellent kinetic study and activation energy of the reaction when two or more elements reacts as a linear temperature is ramped. This allows for a quicker and correct characterization of thin solid state reactions. [59-60].

Theron et al. (1998) used in-situ real-time RBS to study marker motion during $CrSi_2$ formation in the $Si/Pd_2Si/Cr$ system. They compared results obtained using in situ, real-time isothermal anneals and ramped temperature anneals with those obtained by other authors using

34

conventional annealing. They made other example which involved the use of an inert Tantalum marker to determine the origin of Silicon supply when $CrSi_2$ is formed on top of Pd_2Si. They annealed and analysed samples in situ and RBS spectra were obtained with 2 MeV alpha particles using a backscattering angle of 165° and tilting the sample 10° towards the detector. RBS spectra were obtained continuously and accumulated spectra stored at regular intervals (every 10 s). As reported, they annealed the first set isothermally at a number of temperatures ranging from about 195 °C to 320 °C and the samples of the second set annealed at different ramp rates ranging from 0.1 to 30 K/min. Fig. 2.21 shows in-situ real-time RBS spectra of the formation of CrSi2 on Pd2Si at 425 °C [60].
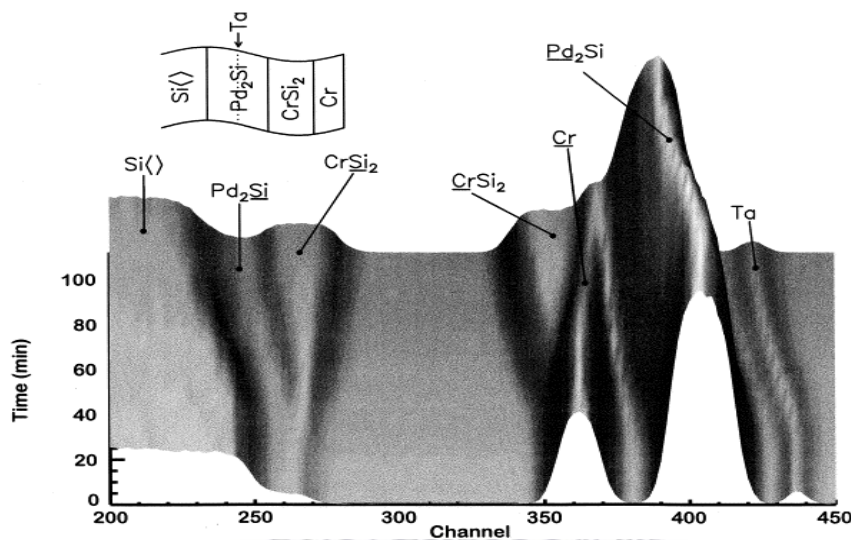
Fig. 2.21. *In situ, real-time RBS spectra of the formation of CrSi2 on Pd2Si at 425°C [60]*

The real-time RBS analysis clearly showed that some Pd_2Si must have dissociated although this only occurred during the initial stages of $CrSi_2$ formation. In this study it was illustrated by the measurement of the reaction kinetics of Pd_2Si formation that real time RBS can study reactions. The activation energy and pre-exponential component should be acquired from a single sample by way of ramping the temperature, whilst continuously carrying out RBS measurements [60].

Mtshali et al. (2019) used real-time RBS to investigate diffusion kinetics and stoichiometric evolution using 2 MeV He$^+$ ions on Silicon-Titanium-Cobalt thin film samples. The thermal annealing was carried out with linear temperature ramping from room temperature to 350 °C

35

at 20 ℃ per minute and from 350 ℃ to 650 ℃ at 3 ℃ per minute. One sample was (as-deposited) and another was first annealed at 450 ℃ under argon gas flow for three hours to kick-start the reaction before the real-time RBS experiment. They found out that the diffusion of the elements could be tracked as the temperature is ramped up [114].

2.7.2. Femtosecond laser annealing

A femtosecond laser is defined as a laser which emits optical ultra-short pulses with a duration in the domain of femtoseconds (10^{-15} s) with a known spot size [61]. Ultra short pulsed lasers overcome some shortcoming of long pulses laser system for micro and/or nano-scale fabrication.
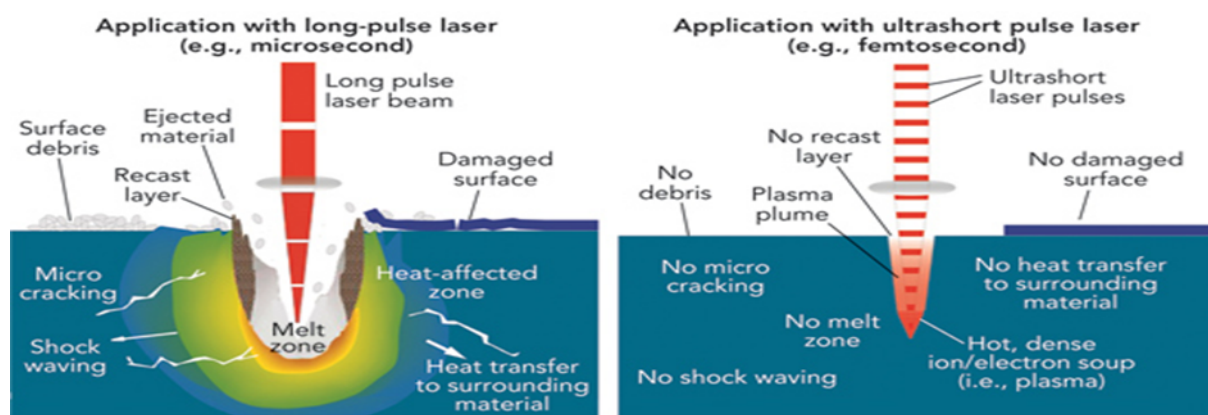
Fig. 2.22. Ultra Short and Long laser pulses [62]

In femtosecond laser pulses according to Fig. 2.22, there is less thermal processing compared to short-pulse laser (which include nanosecond pulses and microsecond) and hence ultra-short pulses have advantages over long laser pulses. Another advantage of ultra-short laser pulses is the reduced heat impact. When a material is constantly annealed using long pulses it gradually loses its original structure and changes characteristics because of the increased heat impact compared to ultra-short. Femtosecond laser has less damage on the surface of the material as it is highly collimated with short and fast pulses. Evidently, in the diagram above in short pulses there is no heat transfer to surrounding material while in long pulses the heat is severely transferred. Furthermore, in long pulses there is melt zone while it's not available in short pulse. Long pulse duration results in greater peak torque, normalized torque, as well as torque-time integral. The pulse repetition rate is the number of pulses emitted per second [61,62].

Studies using lasers have been undertaken with different laser types and pulse regimes with femtosecond laser being utilized for ultrafast pulse related projects [35,63]. Tong et al. (2007) studied the effect of the laser fluency on structural and optical characterization of thin CdS films synthesized by femtosecond pulsed laser deposition with a laser incident energy in the range 0.5–1.5 mJ/pulse. A femtosecond pulsed Ti: Sapphire laser composed of a pulse stretcher with a regenerative amplifier was focused on a rotating CdS target. The laser had a pulse frequency of 1 kHz, beam diameter of 8 mm and it emitted 90 fs pulses at a central wavelength of 800 nm. The XRD results from this study showed that CdS thin films are dominantly hexagonal structure. They also reported that by increasing the laser incident energy from 0.5 to 1.2 mJ/pulse the intensity of the CdS diffraction peaks appeared more intense and sharper. Another observation was that when the laser incident energy was raised to 1.5 mJ/pulse, the intensity of CdS diffraction peaks became slightly weak which indicated that the crystalline quality of the CdS thin films slightly decreased. The CdS thin film deposited at the laser incident energy of 1.2 mJ/pulse displayed relatively good structure and optical properties. The results from this study have shown that crystallinity, surface quality and the optical characteristics of the CdS thin films are strongly dependent on the laser incident energy [63].

Zhu et al. (2015) used an amplified Ti:sapphire laser system with the incident laser beam perpendicular to the surface to irradiate Si. Laser incident energy of 6 mJ/pulse at a wavelength 800 nm wavelength was used and the average laser fluency was controlled by laser beam splitters. The study revealed that femtosecond laser irradiation on Si solid leads to the formation of a composite of nano-crystalline, amorphous and Si substrate surface with microstructures. The transformations between crystalline Si and amorphous Si with the femtosecond pulse laser irradiation may provide a new method to make low cost infra-red Si detectors [64]. Shao-Xu et al. (2012) investigated the effect of femtosecond laser irradiation and subsequent thermal annealing on the electronic, optical, and optoelectronic properties of silicon supersaturated with sulphur by ion implantation. When conducting experiments, the focused laser spot was 350 μm in diameter and was exposed to an average of 480 pulses. The implanted samples were thermally annealed in N_2 for 30 min at 825 K after femtosecond laser irradiation. Some ion implanted samples without laser irradiation were also annealed at different temperatures for comparison. Femtosecond laser irradiation and subsequent thermal annealing can electrically and optically activate the supersaturated sulphur in silicon, and improve the photodiode fabricated from the laser-irradiated sample [65]. Neimash et al. (2016) performed a study where laser light at relatively low power was used to initiate and sustain the process of Sn-induced

crystallization. Laser annealing was proven to supply the opportunity of fine-tuning the nano crystals size and concentration, which is important in photovoltaic and thermoelectric devices fabrication. The local temperature within the laser spot and duration of the heating process control the formation rate, size and concentration of Si nanocrystals and, therefore, depend on the irradiation power and exposure time to laser radiation. Fig. 2.23 shows the SEM micrographs for the analysed selected region of interest from this work.
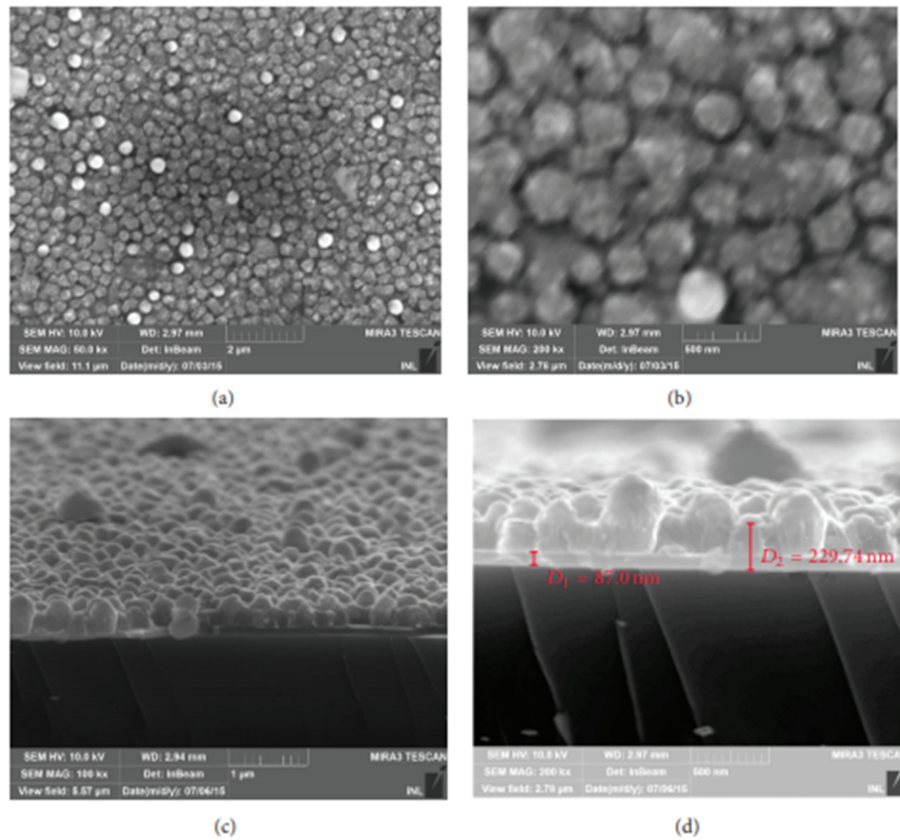
Fig. 2.23. SEM images of the 3-layer structure Si/Sn/Si. The thicknesses of the deposited layers were X: Y:Z = 100: 50: 100 nm. Panels (a) and (b) are images of the surface with different magnification. Panels (c) and (d) are tilted images of the chipped surface [95].

The light reflection from the surface of the sample was reportedly negligible because of the surface morphology of the sample shown in the figure above. Evidently from Fig. 2.11, the surface appeared like black soot, featuring thereby significant property of energy loss minimization due to reflection, which has proved to be important for the solar cells industry. The results showed that Si nanocrystals formation rate, their size, and concentration are controlled by the local temperature within the laser spot and duration of the heating process and, therefore, depend on the irradiation power and exposure time to laser radiation [95].

2.8. Characterization techniques

2.8.1. Field Emission Scanning Electron Microscope

Field emission scanning electron microscope (FE-SEM) is a type of a microscope which uses a focused beam of electrons to scan a surface of a sample to create a high-resolution image. FE-SEM produces magnified images of an object being measured with the features of the sample highly resolved. This high resolution is achieved due to the short wavelength nature of the electrons which is much smaller than those of light [115]. The effect of the wavelength of the probing matter can be demonstrated by the Abbe equation;

$$d = \frac{\lambda}{2nSin\theta}$$

(1)

Where d is the resolvable feature size, which could be the distance between two object or particles on the sample, λ is the wavelength of the probing particles (electrons) n is the index of refraction of the medium and θ is the half angle of the converging spot on the sample from the lens. The denominator of equation 1 is a representation of a lens numerical aperture and the simplified equation is;

$$d = \frac{\lambda}{2}$$

(2)

The resolution of the features of the sample being measured are limited by the wavelength because the shorter the wavelength the greater the resolution. The limit of resolution is also affected by the aberration of the lens and the coherence of the probing electrons.

2.8.1.1. Sample characterization using FE-SEM

A beam of electrons in the FE-SEM is generated using a field emission gun by applying a high potential difference between a Müller type Schottky emitter. A negative potential relative to the electrode creates a gradient for the electron to accelerate through to the samples. The advantage of field emission gun is its high brightness which have an influence on the resolution

[116]. The FE-SEM used was used for morphological characterization of Zn-Mo thin films. A beam of electrons is channelled down the evacuated chamber through a pin hole aperture just below the emission gun and these monoenergetic and coherent electrons are shaped by a series of electromagnetic lenses (condenser lens and objective lens). Once the electrons interact with the sample signals ranging from secondary electrons, backscattered electrons and X-rays can be generated and these are detected via detectors. The detector creates snap shots which are displayed on a computer display screen. Fig.2.24 shows a schematic representation of the interaction of the electrons in the SEM and the signal generated.
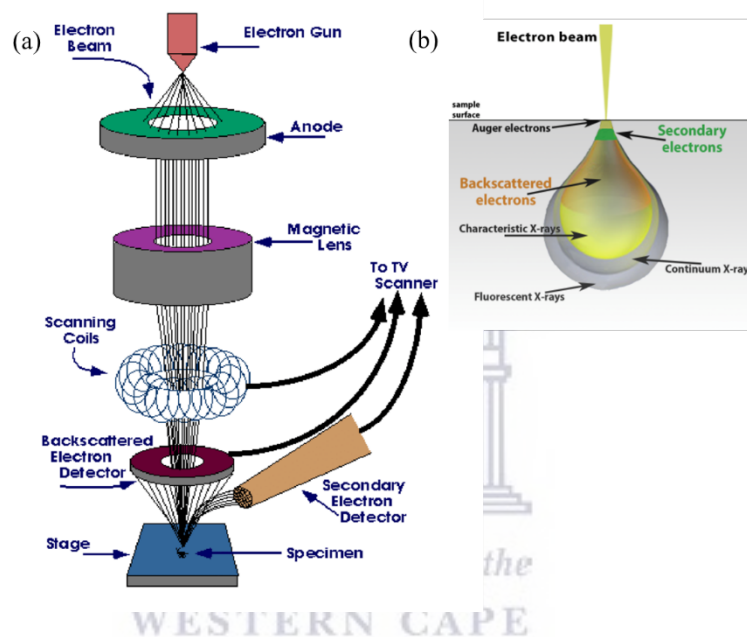
Fig. 2.24. (a) Signals produced during the electron beam-specimen interaction in the SEM microscope and (b) the regions from which the signals can be detected [71].

Characteristic X-rays and Auger electrons determine chemical composition, while backscattered electrons are necessary to demonstrate contrasts with regards to composition in multiple specimen (using atomic number). Secondary electrons provide topographical information of the specimen [66-70].

40

2.8.2. X-ray diffraction (XRD)

XRD is a non-destructive analytical technique used in order to obtain crystallographic information of a material. The technique is based on the interaction of monochromatic X-rays and the periodic crystal lattice of a material. The energy and incidence angle of the X-rays and the electron density of the sample influence the penetration depth of X-rays. With this technique, only information about the crystal grains near the surface can be analysed and this is because X-rays will only penetrate the surface of the material, reaching a few μm into the material [74-77].

2.8.2.1. X-ray diffraction principle

XRD instrument is equipped with an X-ray tube from which the X-rays are extracted and directed towards the sample. When the X-ray photons interact with the sample the photons react with the material in several different ways, however in XRD only the diffracted photons are of interest [ref]. During diffraction the X-rays become scattered on the different crystal planes of the sample material and the diffracted rays are recorded by the detector for analysis. X-rays interact with the lattice when propagating through a crystal of the sample and are diffracted according to Bragg's law equation below. Diffraction of X-rays by the elastic scattering leads to formation of diffraction patterns. The combination of constituent atoms, crystal structure, and lattice constants is different for every material or phases and as a result unique set of diffracted intensities are produced making the phase identification process possible [78,79]. The mathematical expression of Bragg's law is stated in Eq. 3 and the schematic representation in Fig. 2.25.

$$n\lambda = 2dSin\theta$$

(3)

Where n is the integer, λ is the X-ray wavelength, d is the crystal plane spacing and θ is the angle between the incident X-rays and the crystal plane.
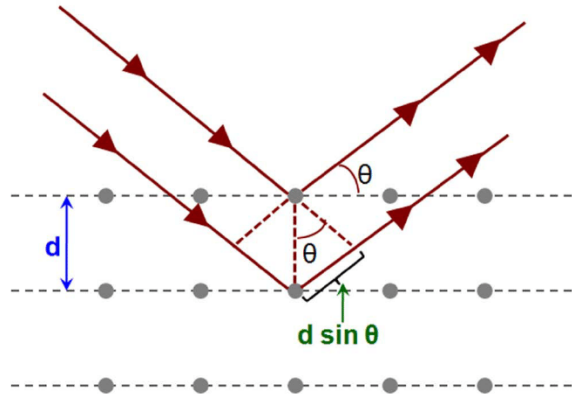
Fig. 2.25. *Schematic representation of Bragg's law of diffraction of X-rays.*

Bragg's law states that a constructive interference occurs when the spacing, d is equal to $n\lambda$ (a whole number, n of wavelength). When the X-ray is incident onto a crystal surface its incident and scattering angle are equal [80]. In the current study XRD experiments were conducted using a Bruker D8-Advance-8 advance X-ray diffractometer.

2.8.3. Rutherford backscattering spectrometry (RBS)

RBS is a widely used non-destructive ion beam analysis technique for elemental composition determination, impurity distribution, depth profiling and areal density. This technique uses helium ions (He^+) of MeV energy to probe the sample under investigation. The alpha beam is produced by particle accelerator and the beam is then collimated and filtered using a series of electromagnetic magnets along the beam line. The energy range of alpha particles used in the RBS analysis is between 0.5 to 6 MeV. During interaction between the sample and alpha beam, the incoming charged particles are backscattered from the atoms in the near - surface region of the sample and the experimental setup is presented in Fig. 2.26.
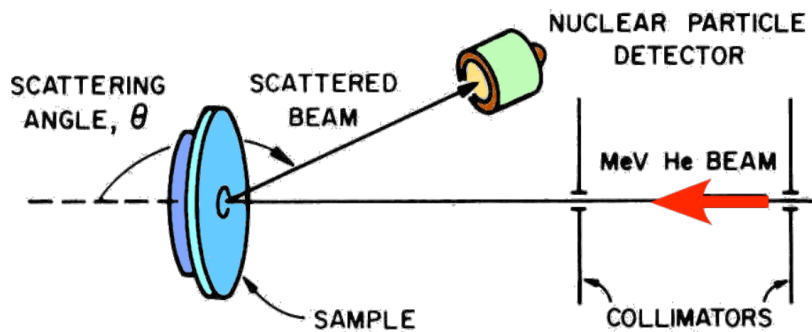
When the alpha particles strike the target sample some particles are backscattered and detected using silicon surface barrier detector. The detector is placed at the backscattering angle as large as possible to collect the largest number of scattered ions. The detector signal is then magnified and reshaped in the preamplifier. The detector and preamplifier are powered by the electronic equipment which then stores data in the form of backscattering spectra [81-83].

In RBS, the interaction between the alpha particles and the atoms of the sample is governed by kinetic factor, energy loss and differential scattering cross section.

2.8.3.1. Kinematic Factor

The kinematic factor is described as the ratio of the incident energy after an elastic collision to that before the collision. The interaction between the incident particles with target atoms is considered an elastic collision which obeys laws of conservation of momentum and energy [84]. Fig. 2.27 below illustrates elastic collision between a projectile of mass M_1 and the target atoms of mass M_2. For scattering that occurred at the surface of the sample, the only energy loss is due to the momentum transferred to the atoms of the target material and the kinematic factor is given by Eq. 4.
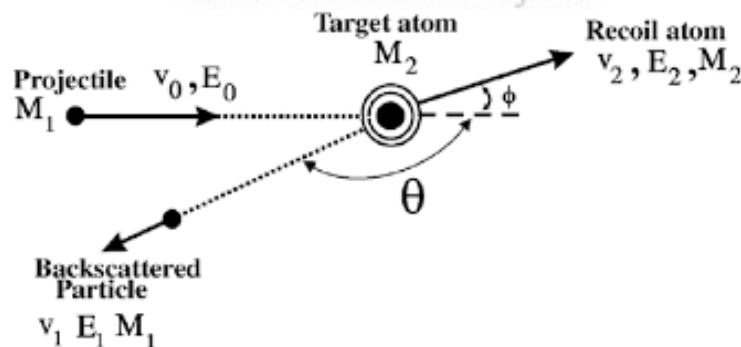
Fig. 2.27. Elastic collision between a projectile of mass M₁ and the target atoms of mass M₂ [88]

The ration k of the projectile energy during collision between an incident energetic particle M_1, with M_2 is described as $K = E_1/E_2$. Since the collision is considered to be elastic, both energy

and momentum are constant and therefore the ratio of projectile's energy can be determined for $M_1 < M_2$ as;

$$\frac{E_1}{E_2} = K = \left[\frac{\left(M_2{}^2 - M_1{}^2 \sin \sin \theta^{\,2}\right)^{\frac{1}{2}} + M_1 \cos \cos \theta}{M_1 + M_2} \right]^2$$

(4)

Where M_1 is the mass of the incident particle, M_2 is the mass of the target atom and θ_1 and θ_2 are defined as the angle between the incident ion before and after scattering. The kinematic factor is a function of M_1, M_2 and θ only. From the equation it can be deduced that the energy of scattered projectile by heavier elements is higher than those scattered by the lighter elements.

The significance of the kinematic factor is that by measuring the energy backscattered, one can determine or identity the mass of the target atom [81]. The preferred position of the detector for backscattered particles is at an angle of 180°. The graph in Fig. 2.28 shows kinematic factor for a scattering angle 165° as a function of the target mass M_2 for different beam particles. The kinematic factor which is the ratio E_1/E_0 becomes constant as the mass M_2 of target increases for different incident atoms.
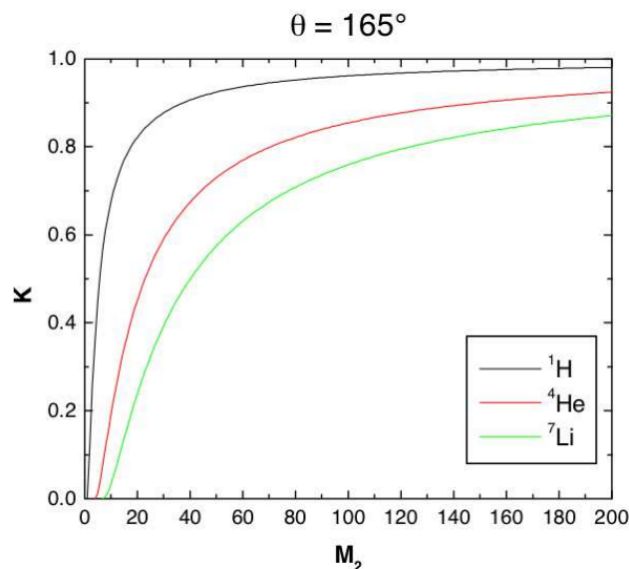
Fig.2.28. *Graph shows kinematic factor for a scattering angle 165° as a function of the target mass M_2 for different beam particles of Lithium, Helium and Hydrogen ions [81].*

2.8.3.2. RBS differential scattering cross section

When the incident particles interact with target atoms, incident atoms experience collisions and loose energy during that collision. Scattering cross-section is a parameter that defines the extent and probability of the collisions. This parameter is described in terms of a differential cross section $\left(\frac{d\sigma}{d\Omega}\right)$ which is the relative number of backscattered atoms into a detector's solid angle $d\Omega$ for a given flux of incident particles. The scattering cross section is given as:

$$\frac{d\sigma(\theta)}{d\Omega} = \left(\frac{Z_1 Z_2 e^2}{4E}\right)^2 \frac{4}{sin^4\theta} \frac{\left\{\left[1 - \left(\left(\frac{M_1}{M_2}\right)sin\theta\right)^2\right]^{1/2} + cos\theta\right\}^2}{\left[1 - \left(\left(\frac{M_1}{M_2}\right)sin\theta\right)^2\right]^{1/2}}$$

(5)

Where z_1 and z_2 are atomic masses of the projectile atom with M_1 and target atom with M_2 respectively. The equation shows that the probability of scattering is inversely proportional to the square of the incident energy and therefore as the energy of the projectile decreases the probability of scattering increases. The scattering cross section is much greater at small angles [85,86]. The scattering cross section have an influence on the yield and shape of the spectrum and spectrum yield of backscattered particles is given by equation:

$$Y = \sigma(\theta_1)\Omega Q N \Delta t / cos\theta_2$$

(6)

Where $\sigma(\theta_1)$ is the scattering cross-section at angle θ and Ω is the detector solid angle. Q is the number of incident particles and N is the atomic density, Δt is the thickness of target and θ_2 is the angle between the incident beam and the target surface.

2.8.3.3. Energy loss and stopping power

During beam interaction with the target sample, the incident ions lose energy when traversing the material which leads to deceleration of the ions before and after collision. The deceleration of ions in the target material is described as the stopping power, which enables the

45

determination of the elemental depth distribution. A projectile with energy E striking on a target, will penetrate into it and kinetic energy of the projectile decreases. The amount of energy lost per distance Δx traversed depends on the identity of the projective, and the density and composition of the target [81,87].
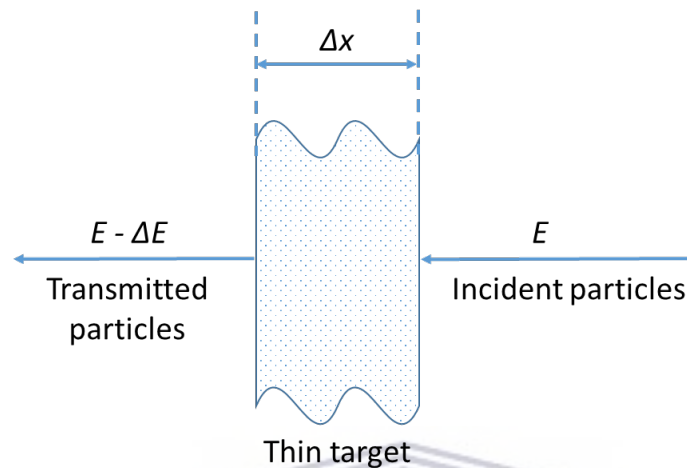
Fig. 2.29. *Illustration of energy loss per distance Δx traversed through a thin target.*

The diagram in Fig. 2.29 illustrates the beam of energy E impinging the target and losing energy as it traverses. ΔE is the energy lost as it traverses distance Δx into a target of electron density n, and energy of the transmitted particle is E-ΔE. The energy loss per unit length dE/dx at the energy E of the incident projectile is defined using the formula:

$$\frac{\Delta E}{\Delta x} \equiv \frac{dE}{dx}\,(E)$$

(7)

The accuracy of the stopping cross section have an influence on determination of target thickness and depth profile measurement by RBS [81,87,88].

2.8.4 Atomic Force Microscope (AFM)

AFM is a technique used in the surface analysis of rigid material down to the level of the atom. This technique uses a mechanical probe to magnify surface features and produces 3 dimensional images of the surface [89]. A typical AFM system set up is comprised of a cantilever with an extremely sharp tip, a scanner, a sample stage, laser and a photodiode

46

detector as depicted in Fig. 2.30. AFM operate on the principle of surface sensing using a sharp tip mounted at the end of a cantilever. The tip bends in response to the force exerted on the tip by the sample and is used to image the target sample by raster scanning across the surface line by line.

AFM has two general modes of operation which are the static mode also known as the contact mode and the dynamic mode which is refers to the non-contact and the tapping mode. In each of the modes there are dominant interaction forces which give information about the topography of the sample. The repulsive forces are seen in the contact mode and the attractive forces in the non-contact mode. In the tapping mode at high frequencies both the repulsive and the attractive forces are experienced. In tapping mode, the probe makes the contact with the sample at regular intervals. In contact mode there is a constant slight contact between the sample and the probe which maintains the contact force. The mode is dependent on the type of sample to be measured and physical characteristics to be studied [89-91]. The applied forces during the interaction between the AFM tip and the samples surface are attractive or repulsive depending on the distance between the tip and the sample. The force is attractive if the distance is big enough and repulsive if it is small due to overlapping of electron orbitals between tip and sample. Contact mode AFM has repulsive interaction forces, non-contact with attractive van de Waals forces and the tapping mode using vibrating tip to examine the surface. The tip position gives a three-dimensional image of the sample surface and the contours of the tip - sample force closely follow the surface topography [92-94].
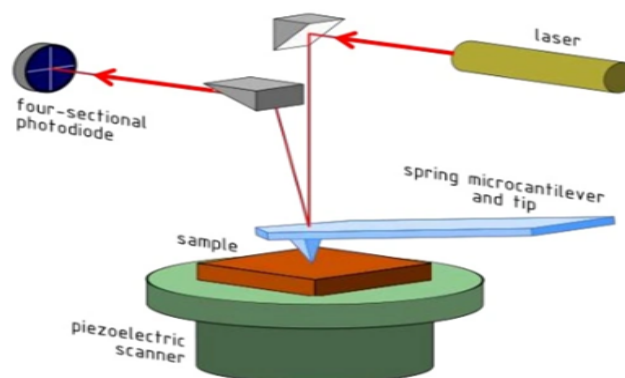
Fig. 2.30. *Operation principle of atomic force microscopy* [93]

47

The sample surface topography image is acquired using a feedback mechanism that enables the scanners to maintain the tip at constant force or tapping mode above the sample surface. A cantilever attached to a probe monitors the force and the higher the cantilever deflection the higher the force experienced by the probe.

CHAPTER 3: RESEARCH METHODOLOGY

3.1 Introduction

A bi-layer of Zn and Mo thin films were prepared using electron beam evaporation system. In this chapter, a detailed description on sample preparation and characterization techniques used to study Zn-Mo thin films deposited on substrates will be presented. Thin film analysis is accomplished through logical utilization of different characterization techniques which are discussed in details throughout the chapter. Samples roughness and topography were analysed using AFM and XRD was used to study the microstructures and to identity crystallographic phases formed. Morphological structure of the samples was examined using scanning field emission SEM. RBS technique was used for determination of materials thickness, depth profile and diffusion mechanism and program software SIMNRA was used for simulation of the experimental data.

3.2. Deposition of Zinc and Molybdenum thin films

A thin bi-layer of Zn and Mo were deposited using electron beam evaporation system in Fig. 3.1 (a). Before deposition the electron beam evaporator chamber was pumped down to base pressure of 1×10^{-7} mbar. This was achieved by first pumping down the chamber using rotary pump followed by a turbo pump. When the pressure reached 1×10^{-5} mbar, titanium sublimation pump cooled by liquid nitrogen was deployed to further improve the vacuum to a base pressure of 1×10^{-7} mbar. Once this base pressure was reached, the target materials were then de-gassed using the electron beam, this was done to remove any residual adsorbed atmospheric gasses that were not pumped out. The system has a crucible shutter placed between the evaporant vapour source and the substrate holder which is used to stop the deposition by closing it when the desired thickness is achieved. The amount of thickness deposited and deposition rate are monitored through a crystal balance monitor controller mounted close to the substrate. Evaporation process and parameters were controlled and monitored using controls in Fig. 3.1 (b).

Once this procedure was completed the target materials were evaporated and deposited at a rate between 2.4 and 1.2 Å/s and the substrate temperature was set to room temperature. The evaporation process was monitored using a thin film monitor.
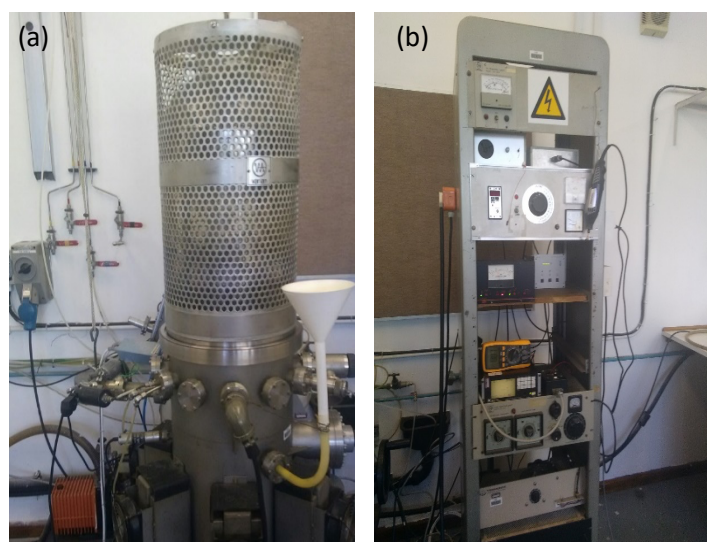
Fig. 3.1. *Electron beam evaporator system setup used for Zn-Mo film deposition*

A beam of electrons was generated from a resistively heated tungsten filament and accelerated towards the target material placed in a crucible. These electrons cause the target material to evaporate and as the vapour impinges the surface, the gas (hot vapour) molecule may lose enough kinetic energy during collision with the substrate surface atoms forming chemical bond with atoms of the substrate. The mobility of the atoms on the surface of the sample is higher and therefore they are settling down on equilibrium positions [29]. Atoms of the evaporant are being held and grown as the thin film on the substrate and forming nuclei of different sizes and this is followed by the formation and merging of the critical nuclei to form one mass (coalescence) of film.

3.3. X-ray diffraction measurement on Zn-Mo thin films

XRD provides information on the atomic arrangement in materials, crystallographic phases, and crystal orientation (texture). Other crystallographic parameters, such as grain size, strain, lattice parameters and crystal defects can be calculated from the XRD data. External factors such as pressure, temperature and cooling rate during recrystallization can affect the arrangement of atoms in the material. Amorphous solid materials are an assembly of atoms with an irregular atomic arrangement, and have no periodic repetitive structure, while crystalline materials, have atoms that are arranged in regular and repeated pattern [72-73].

The Bruker AXS D8 ADVANCE X-ray diffractometer was used to study Zn-Mo films. This equipment has a source that produces $CuK_{\alpha 1}$ (with wavelength of $\lambda = 1.5406$ Å) coherent and monochromatic X-rays and it is fitted with a Ni-filter. During the XRD measurements the

50

system was operated at a voltage of 40 kV and a current of 40 mA. The diffraction angle (2θ) was scanned from 30° to 60° with an increment step of 0.01° and the X-ray photons counted for 1 second at each step. The indexing of the Bragg's peak was done using JCPDS catalogue.

3.4. Real-time RBS measurement on Zn-Mo thin films

The solid state reaction of different metallic systems can be easily tracked using only a single sample during one experimental run under real-time RBS. This has a considerable advantageous over other ex-situ set-up. In real-time RBS, the sample is continuously analysed while simultaneously heated at a certain temperature ramp rate to induce phase formation solid state reaction. The information about any changes in composition of the material is derived from a single sample by linear ramped thermal annealing [59-60].

3.045 MeV He^{++} beam was generated using a 3 MV Tandetron accelerator and Fig. 3.2 shows the RBS experimental setup used to investigate Zn-Mo films in the current study. The sample was mounted on the sample stage and tilted 10° towards the detector. In order to measure temperature during annealing thermocouples were connected from the back through a narrow hole so that a tip was located inside the copper below the sample and the detector placed at an angle to measure back scattered particles. In-situ RBS was used to monitor and track reaction dynamics with one Zn-Mo sample.
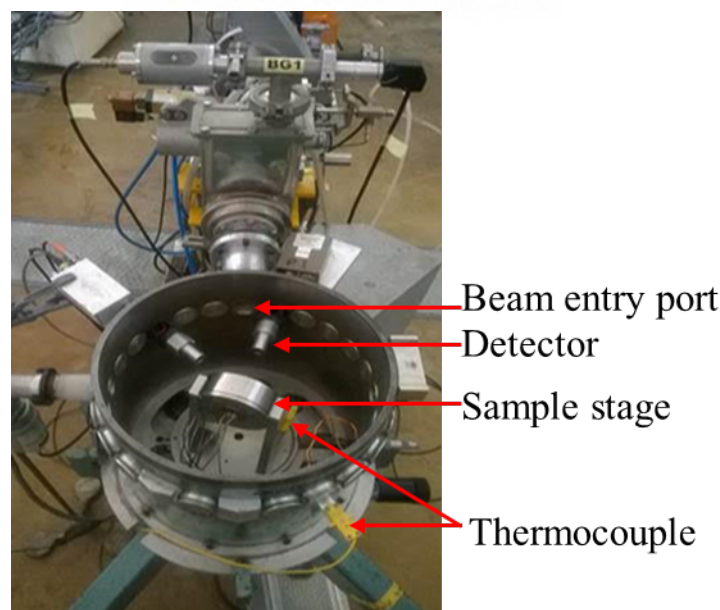
Fig. 3.2. *Scattering chamber with sample stage connected to thermocouple for real-time RBS*

Before the commencement of the experiment the base pressure inside the scattering chamber was pumped to be $1\text{x}10^{-6}$ mbar and monitored in the data room. Zn-Mo bi-layer on a glass substrate was annealed at a ramp rate of 2 ℃/minute from room temperature to 400 ℃. The detection of backscattered alpha particles was achieved by a detector placed at 150° relative to the sample stage and the collected charge was 20 µC.

3.5. AFM measurements on Zn-Mo thin films

AFM is a high resolution microscope that enables the examination of surfaces of materials. This instrument provides quantifiable and accurate surface height, waviness and roughness information, presented in a three-dimensional topographic micrograph. This technique have a great atomic resolution to measure surface roughness in a sub-micrometre scale. The examination of the roughness and topography of Zn and Mo films grown on a substrate was conducted using AFM with a VEECO Nano-scope III shown in Fig. 3.4.

Fig.3.3. *Atomic force microscopy instrument used study the topography of Zn-Mo samples.*

The AFM was operated in tapping mode using Si tips and the frequency of the tip was 10 Hz and the area measured was 25 µm × 25 µm. Roughness analysis and raw data analysis were done using Nano-scope software where the area of choice to be examined was be selected.

3.6 SEM measurements on Zn-Mo thin films

Auriga Ziess field emission scanning electron microscope was used to characterize the surface morphology microstructure of the samples. The sample were loaded in a load-lock of the apparatus which was pumped down to a base pressure before the samples were loaded to ultra-high vacuum pressured analysis chamber for measurements. A field emission gun was operated at a terminal voltage of 5 kV, the electrons were guided down the column of the microscope to the sample stage using both the objective and condenser electromagnetic lenses. The GIMINI 2 Ziess in-lens detector which use both the backscattered electrons and secondary electron was used to generate a micrograph. The working distance of the measurement was set at 5 mm and different magnification ranging from 10 000X to 100 000X were used for imaging.

53

Chapter 4

4.1. Results and discussion

4.1.1. Background

Thin films of Zn deposited on a substrate, (Mo) layer grown on top of Zn, were fabricated using electron beam evaporator. Both the pristine and annealed samples of these metallic bi-layers were studied for their surface morphology using field emission scanning electron microscope (FE-SEM) and atomic force microscope (AFM). The microstructure of both the pristine and annealed samples were analyzed using X-ray diffractometer to determine the crystallographic nature of the materials. These characterization techniques were also used to determine the growth mechanism of both metals while forming a bi-layer.

The reaction kinetics and evolution of the metallic bi-layer thin film during annealing were tracked in real time mode using Rutherford backscattering spectrometry (RBS). This experiment was conducted in a high vacuum RBS chamber using alpha particles as probing particles. This experiment also helped to determine the eutectic temperature of the system and the stoichiometry of the product after annealing.

The advantage of using real-time RBS, was to eliminate the possibility of introducing error in the measurements, by using a single sample to collect all the annealing temperatures RBS spectra in one experimental run.

4.1.2. Morphology and microstructure of Pristine Films

A metallic bi-layer of Zn on silicon substrate with a layer of Mo on top of Zn, was grown using electron beam evaporator. This was achieved by first depositing a thin film of Zn onto a silicon substrate using the deposition conditions in table 1. The electron beam evaporator chamber was first evacuated using rotary pump and turbo pump to a base pressure of 1 x 10^{-7} mbar. The high purity target metals were first de-gassed to remove any traces of ambient gases adsorbed. This was achieved by slightly heating the target metals with the electron beam before shutter that shielded the silicon substrate was opened for deposition. The deposition rate and the thickness of the deposited film was monitored using crystal balance positioned above the sample holder.

Elements	Deposition Pressure (mbar)	Deposition rate (Å/min)	Thickness (Å)	Current (mA)
Zn	2×10^{-6}	3-6	1000	15
Mo	8×10^{-6}	2-4	1000	45

Table 4.1: *Parameters of the deposition of Zn-Mo thin film using electron beam evaporator*

The FE-SEM micrograph of Zn film on a silicon substrate is as shown in Fig. 4.1, it can be observed from the micrograph that the film has many dense grains distributed throughout the surface of the substrate. The Zn crystals seem resemble a hexagonal shape at a close look, with some crystals having a distortion.
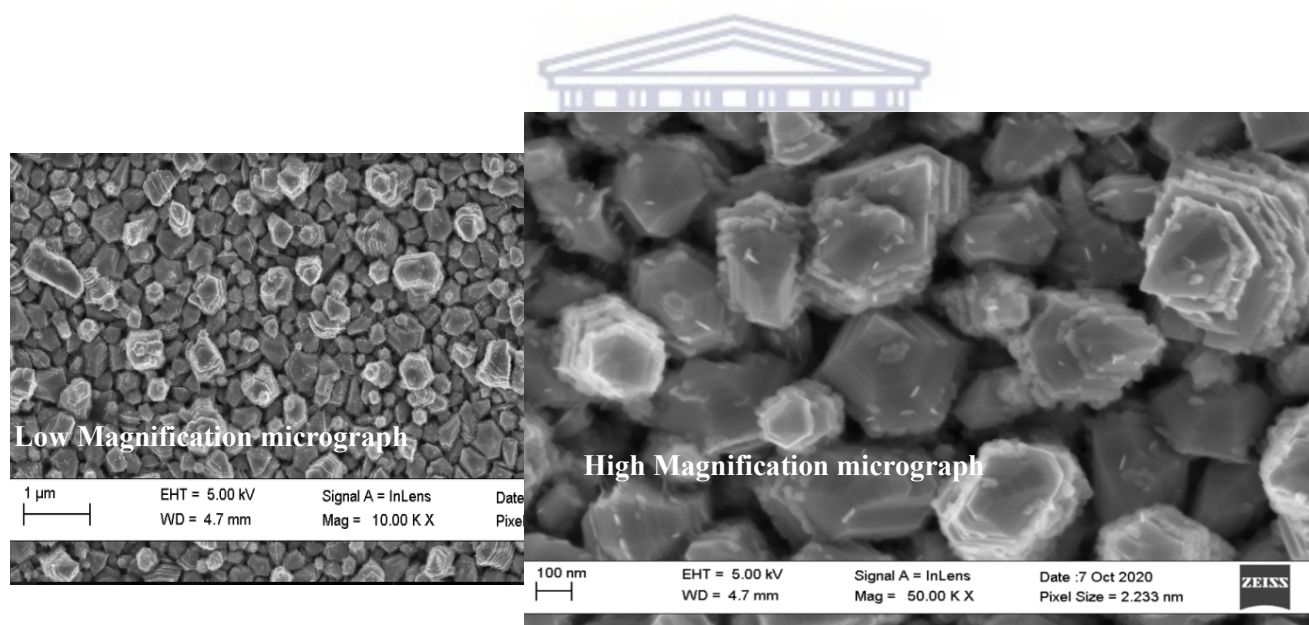
Fig. 4.1. *The FE-SEM micrograph of Zn film on a silicon substrate.*

Atomic force microscope micrograph of the Zn film was measured using the tapping mode, with the canter liver vibrating with a frequency of 10 Hz and the scan area fixed at 10 μm × 10 μm, the root mean square roughness of the film was determined to be 156 nm. The micrograph of the Zn is as shown in Fig. 4.2.

55
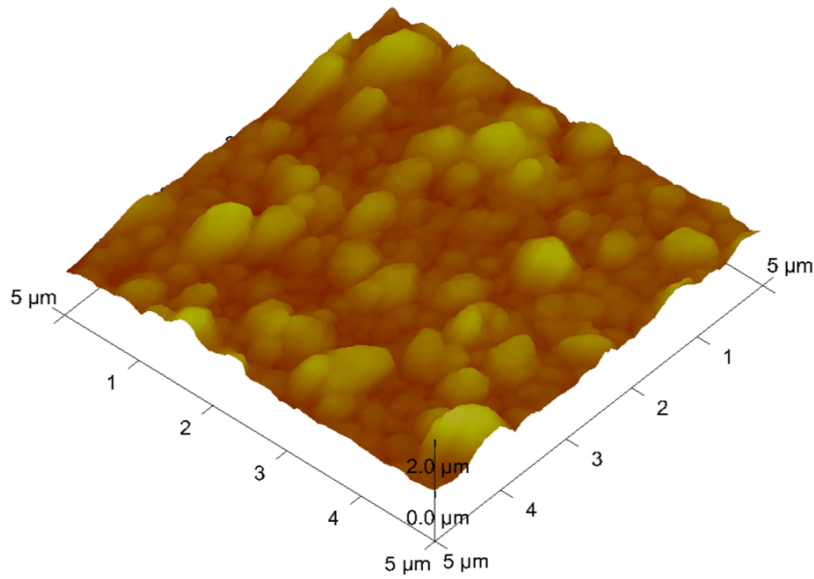
Fig. 4.2 AFM micrograph of a Zn layer deposited using scanning electron beam.

The roughness of the film is representative of the irregular Zn crystal sizes is observed form the FE-SEM micrograph in Fig. 4.1. The microstructure of the Zn film was studied was X-ray diffractometer in θ - 2θ configuration, monochromatic X-ray with a wavelength of 1.54 Å was used to probe the films. The step size of the measurement was set at 0.019 º per second, this measurement was conducted at room temperature. The diffraction pattern of the Zn film is as plotted in Fig. 4.3.
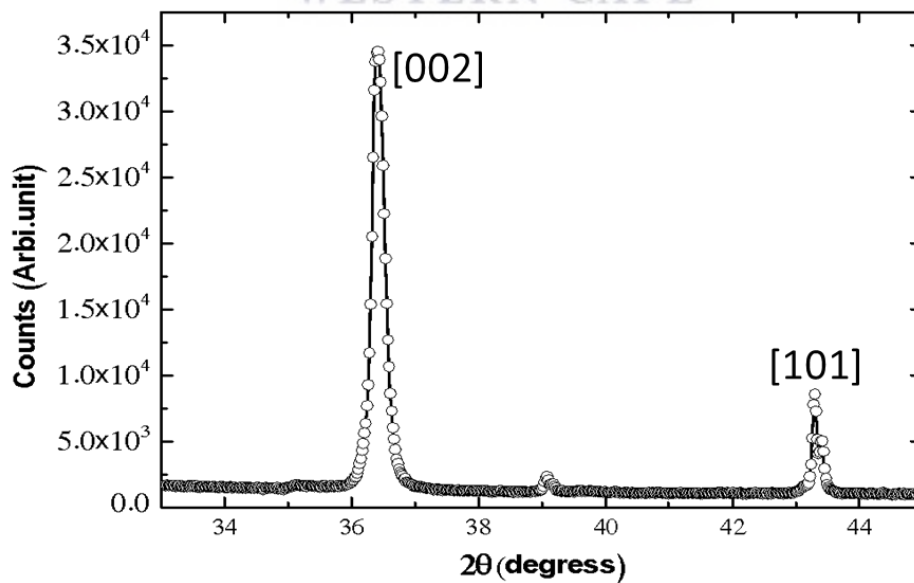
Fig. 4.3. A plot of X-ray diffraction patterns of Zn atom deposited using electron beam evaporator.

The AFM micrograph in Fig. 4.4 exhibit smoother surface morphology, with not much discernable features on the surface. This lead to suggest that the film is more amorphous with a very short ranged ordering of atoms. The root mean square surface roughness was measured to be 4.18 nm. This range of surface roughness suggest that the film followed the Stranski–Krastanov (S-K) growth model with the adatoms coupling with the substrate being stronger than the adatoms to adatoms coupling forces at the beginning of the nucleation and coalescence stage of the growth.
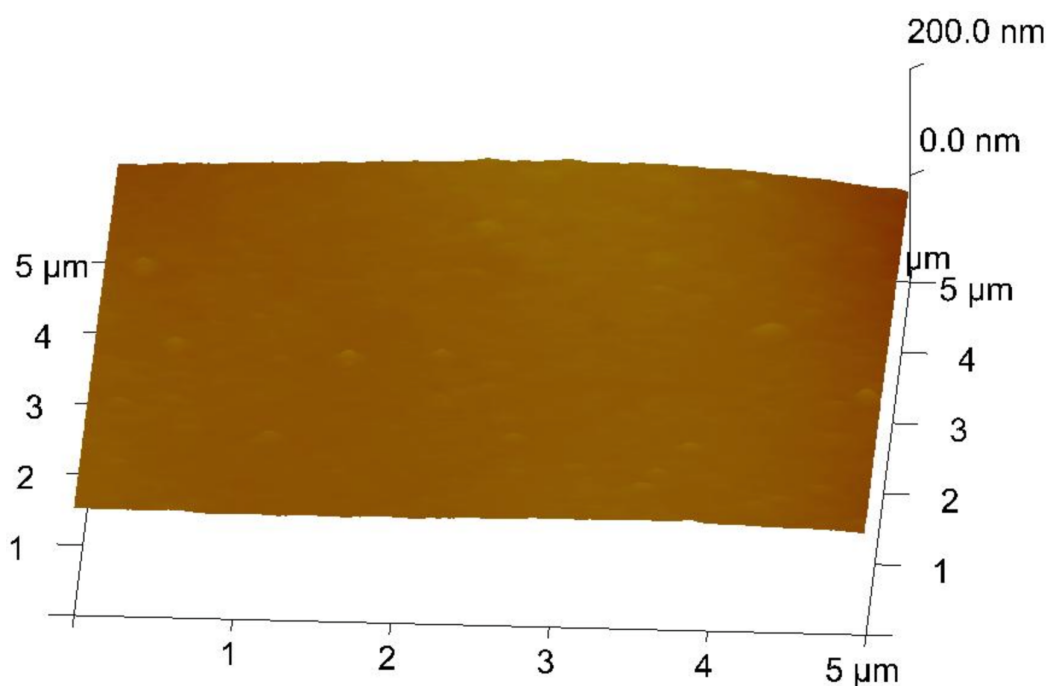
Fig. 4.4. *Atomic force microscope micrograph of Mo film grown by electron beam evaporator.*

The microstructure of the Mo film was studied using X-ray diffractometer, from the plot of the diffraction pattern plot in Fig. 4.5 it is observed that the film is amorphous in nature since there are no discernable Bragg's peak detected from the sample. This result is in line with the AFM micrographs that showed the film to have very small roughness that suggested amorphous film.
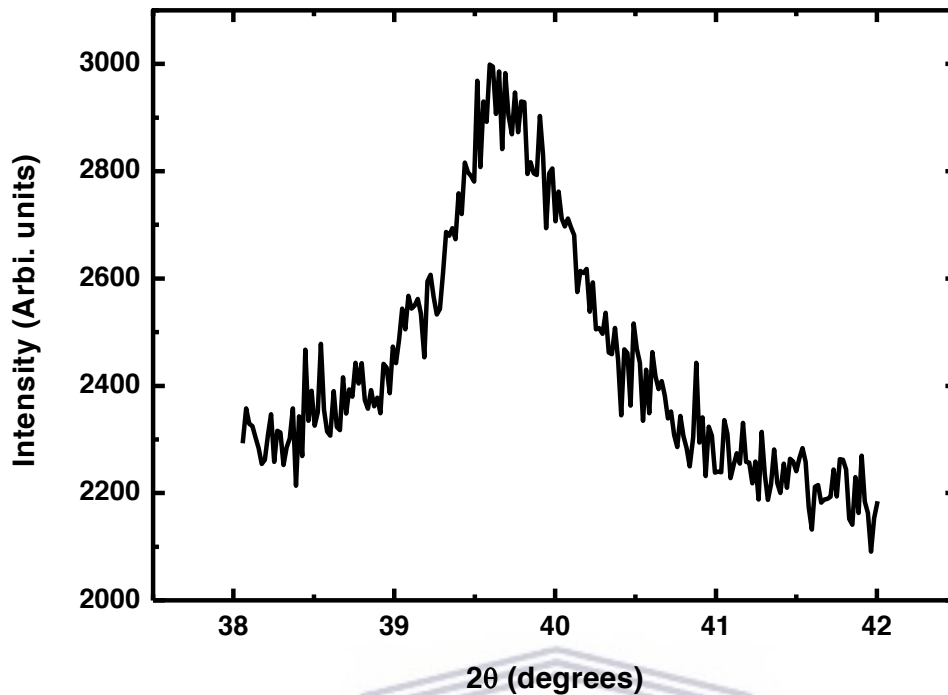
Fig. 4.5 *X-ray diffraction pattern plot of the as-deposited Mo thin film grown by electron beam evaporator.*

4.1.2.1 Bi-metallic thin film study

Mo-Zn thin film was deposited using the electron beam evaporator with the deposition conditions shown in table 1. A layer of Mo was deposited onto Zn after the Zn film was cooled off after deposition. The thickness of each layer was approximately 50 nm, as measured by crystal balance in the deposition chamber.

FE-SEM micrograph of bi-metallic film of Zn-Mo (*Mo on top of Zn*) in Fig.4.6 exhibit rougher crystals with the edges not being as well defines as in the film of Zn only. This is due to the atoms of Mo layer not growing epitaxially onto Zn film, this is because of the strong amorphous nature of the Mo film as observed from the X-ray diffraction microstructure of the film in Fig. 4.5.
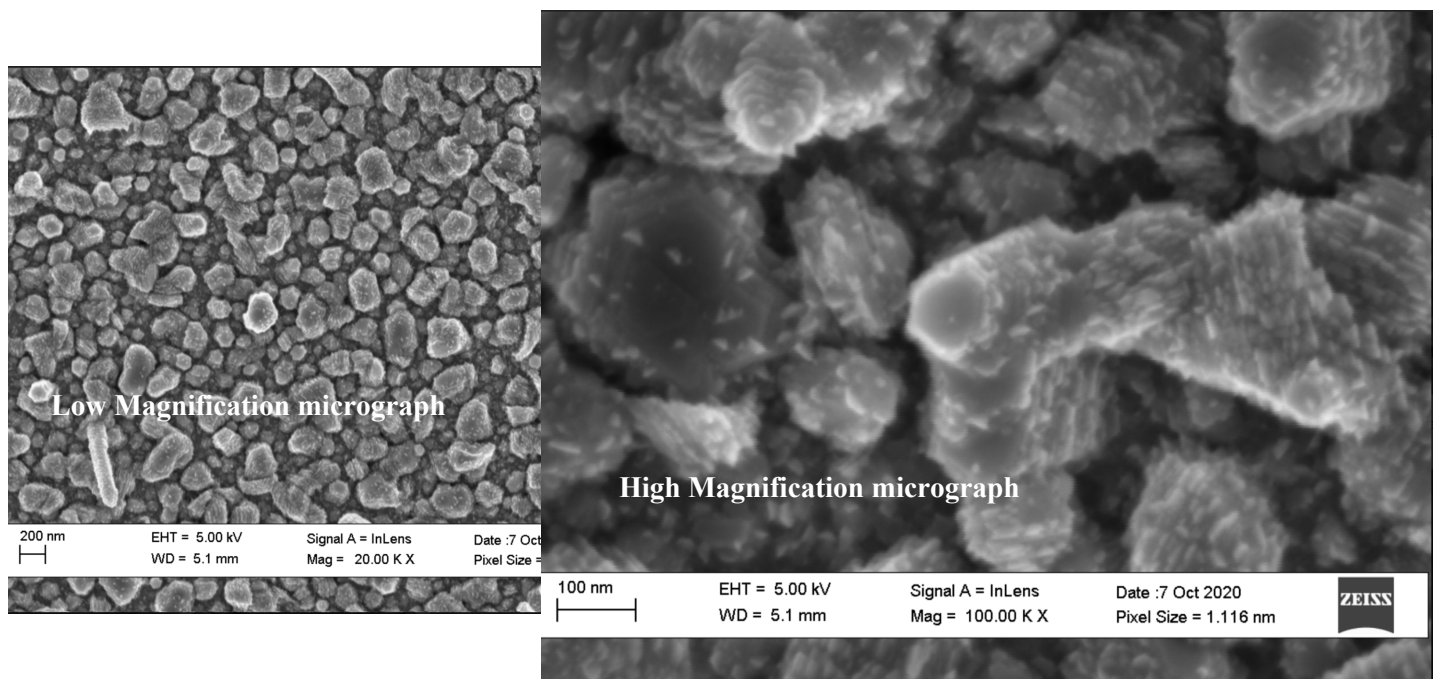
Fig. 4.6. *FE-SEM of bi-metallic film of Zn-Mo grown using electron beam evaporator.*
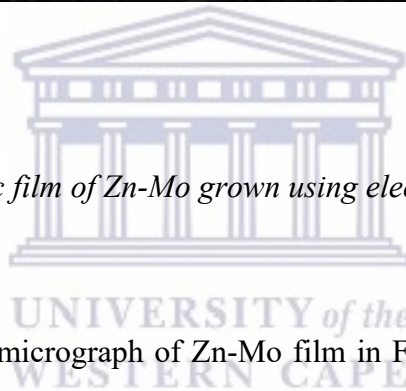
The Atomic force microscope micrograph of Zn-Mo film in Fig.4.7 shows that the film has higher roughness, with the root mean square roughness being 126 nm. The roughness of the bi-metallic film is greater than the roughness of the individual films, this could be as a result of the non-epitaxial growth of Mo onto Zn leading to the crystals that are more distorted.

59
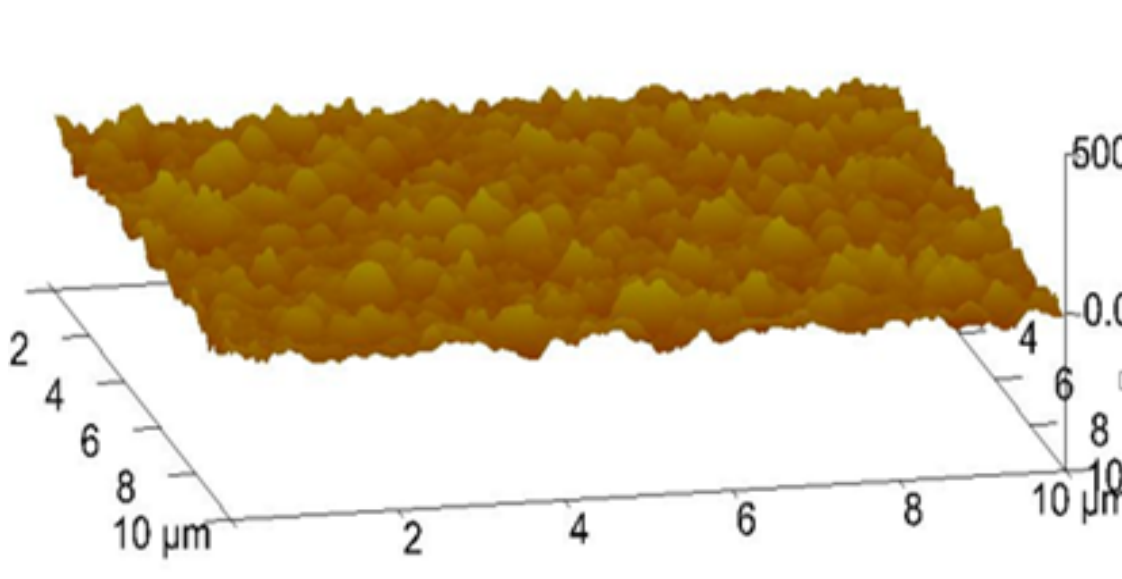
Fig. 4.7. *Atomic force microscope micrograph of Mo-Zn film deposited using electron beam evaporator with Mo as a top layer.*

The Microstructure of the Zn-Mo film was probed using X-ray diffractometer in θ - 2θ configuration, from Fig.4.8, the diffraction pattern plot the Zn-Mo layer, shows Mo to be amorphous, since there is no discernable Bragg's peak that can be detected from the plot. On the other hand, the Zn film has clear Bragg's peak indicating its crystalline nature.
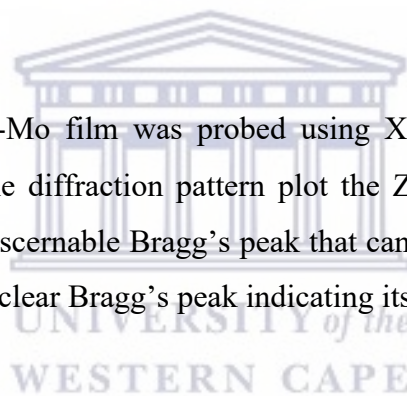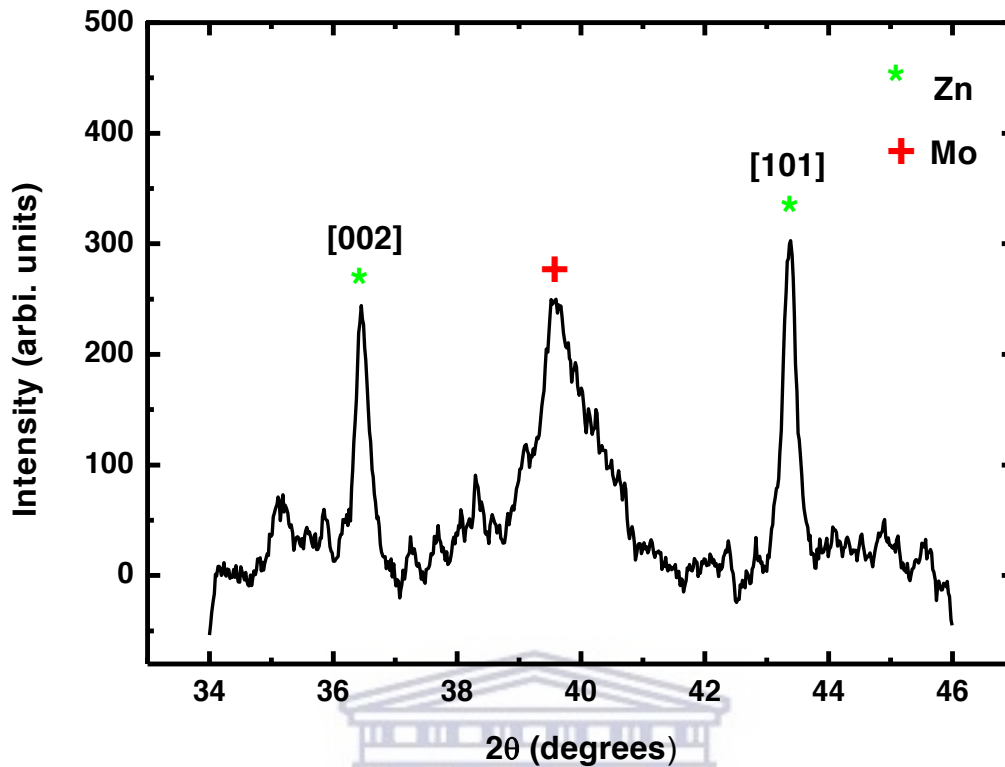
Fig. 4.8. *X-ray diffraction pattern of Mo-Zn film deposited by electron beam evaporator.*

The un-annealed sample structure of Zn-Mo bi-layer films shown slightly larger nanoparticles with greater difference in shapes and many spherical, dense smaller nanoparticles between larger particles. The addition of Mo have resulted to the surface having bigger nanoparticles compared to Zn film only. The morphology and microstructure of Zn-Mo films depends on the Mo content and the substrate used [47]. Figure 4.9 shows AFM results for Zn-Mo bi-layer system on glass substrate in 3-D plotting.
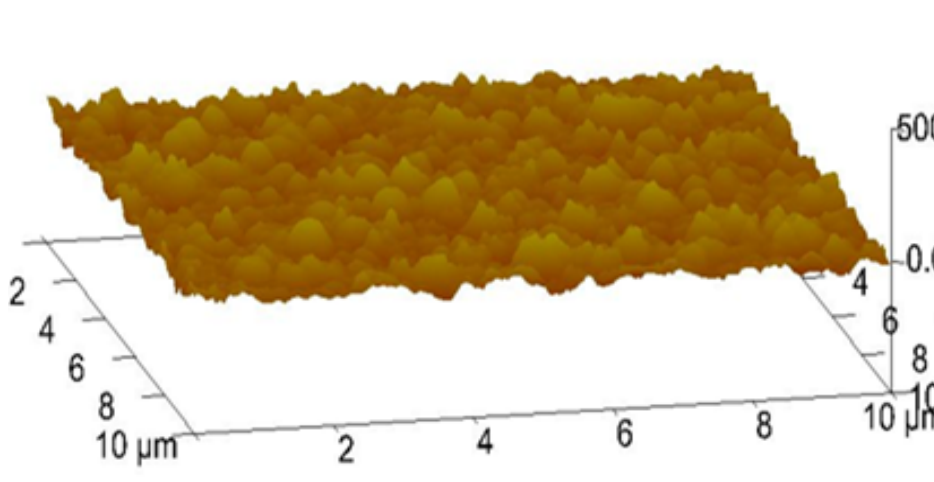
Fig.4.9. *Atomic Force Microscopy results of Mo-Zn deposited by electron beam evaporator.*

From the 5 µm x 5 µm scanned area of as-deposited Zn-Mo bi-layer, the average roughness of the surface is 21.6 nm. The deposition of Mo on top of Zn increases the surface roughness, and thus enhancing corrosion resistance [9].

4.1.3. Real-time RBS analysis of bi-layer film

RBS in an in-situ real-time data collection mode was used to study the atomic depth profile, while heating the sample at a set ramping rate. This heating of the sample was done to induce atomic diffusion and atoms mixing in the sample. This method is advantageous for studying diffusion and the atom mixing of the bi-metallic system, and this is achieved by running a single sample.

Fig. 4.10 shows RBS spectra of the as-deposited Mo-Zn film probed with 3.05 MeV energetic alpha particles from the Tandetron accelerator before annealing. In real-time RBS experiment, the samples undergo a thermal annealing with a ramping rate of 3 ℃/min, from room temperature to 400 ℃. The Chamber pressure was monitored throughout the experiment and the pressure was measured to be 1×10^{-6} mbar. The element with heavy atomic mass appears on high energies and upper channels, while light elements located on low energies and lower channels. High atomic number of an element gives high yield, and low atomic number gives low yield [4].
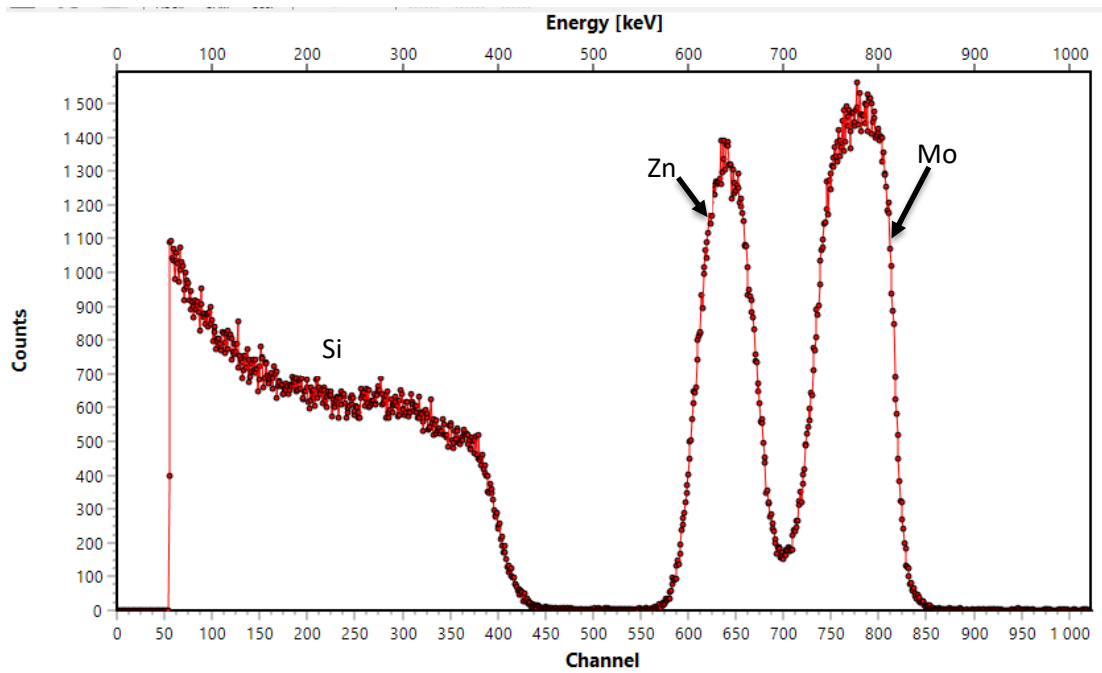
Fig. 4.10. *Normal RBS results of Mo-Zn film before thermal annealing real-time RBS.*

The film thickness can be deduced from the peak width of the spectrum, and elements have their own surface position energy that can help in identifying them, but in a case of bi-metallic systems, elements energies are bound to shift to lower energies due to energy loose during Rutherford backscattering. In this case Mo atoms are on the surface position, and with Zn atoms are below Mo atoms on the second layer, hence the Zn peak is shifted to lower energies on the spectrum. Fig 4.11 shows the collected spectra of the temperature of interest from the thermal annealing of the sample during the real time RBS run.

63
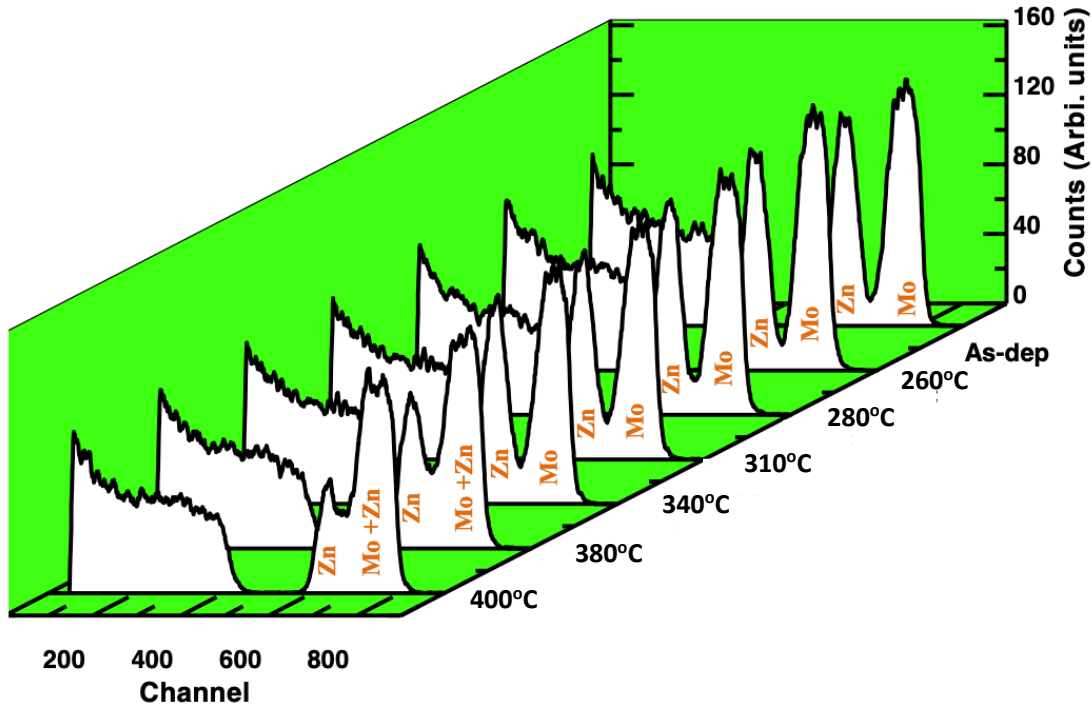
Fig. 4.11. *Collected RBS spectra of Mo-Zn system thermally heated at a ramp rate 3 ᵒC/min.*

From the plot, the evolution of the sample can be observed, this starts with mixing and/or diffusion of the atoms at the film inter-phase as the annealing temperature increases. From Fig. 4.11 it can be suggested that the Zn atoms are interacting with Mo atom as the temperatures increases, this is observed from the Zn peak decreasing in the RBS plot at 340 ℃ and a valley between the two peaks lifting to form shoulder. This phenomenon is indicative of atoms migration though the top layer (*Mo layer*). The width first peak (*Mo peak*) at 246 ℃ appears wider, suggesting the Mo and Zn atoms have mixed forming an alloys, this can be seen the simulation data. As the temperature increases more of the Zn atom are mixed and Mo resulting in further widening of the front peak, with a now mainly Mo (Zn) layer.

The activation energy and the diffusion coefficient of the reaction can be calculated using the Arrhenius plot in a logarithmic format as shown in Eq. 5.

$$lnk = lnA - \frac{E_a}{R}\left(\frac{1}{T}\right)$$

(5)

64

Fig. 4.12 shows a schematic representation depicting the Mo and Zn atoms interaction during thermal annealing at temperatures of interest, as deduced from the RBS spectra in Fig. 4.10 and the related simulation shown in appendix A.
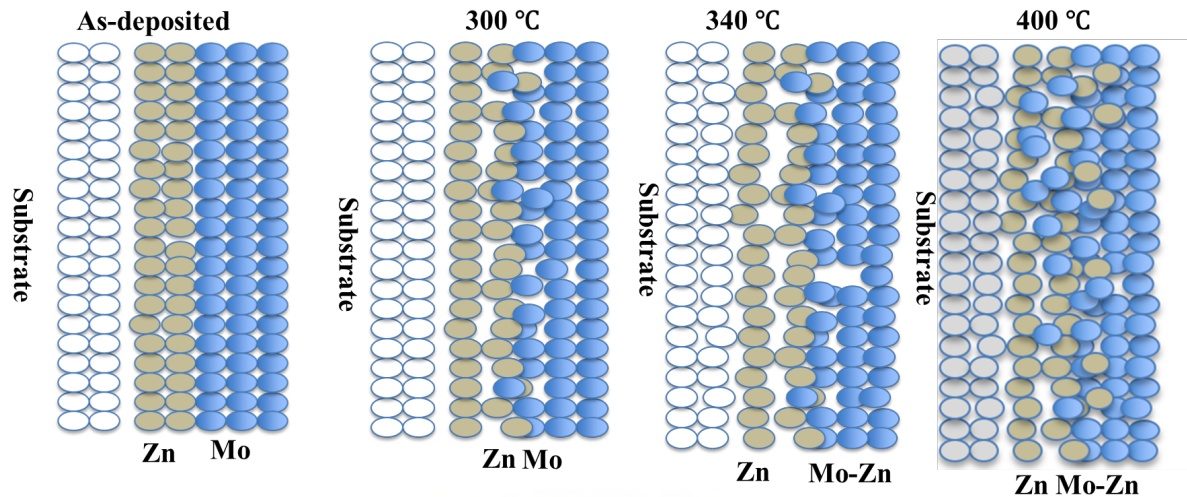
Fig.4.12. *Schematic representation of the Mo-Zn thin evolution and atom migration during thermal annealing in the RBS chamber.*

The sample schematic depiction of atoms migration during thermal heating, give an insight into the diffusion and mixing of the Zn atom, bringing more clarity of the RBS simulation results depth profile.

At temperature 340 ℃ Zn started diffusing through Mo and inter-mixing with the Mo atoms. Some of the Zn atoms started to evaporate off even though there are still more Zn remaining in the sample as shown by the Zn peak on the spectrum. Diffusional breakdown of fully intermixed depositing atoms controls the formation of multiphase structures in alloyed thin films. At very low temperatures there is a lack of atomic mobility leading to single phase structures mostly, and when increasing the temperature there is sufficient mobility for the formation of equilibrium phases.

The spectra obtained throughout the experiment from room temperature to 400 ℃ when annealing using real-time RBS are presented on a contour plot shown in Fig. 4.13, with three distinct bands representing Mo, Zn and Silicon substrate in the system. The difference in the peak height is represented by different colours in the contour plot with red representing the

areas with the highest counts, the green representing the area with the lowest counts than red and blue the lowest counts. The yellow line is the height between the red and green lines.
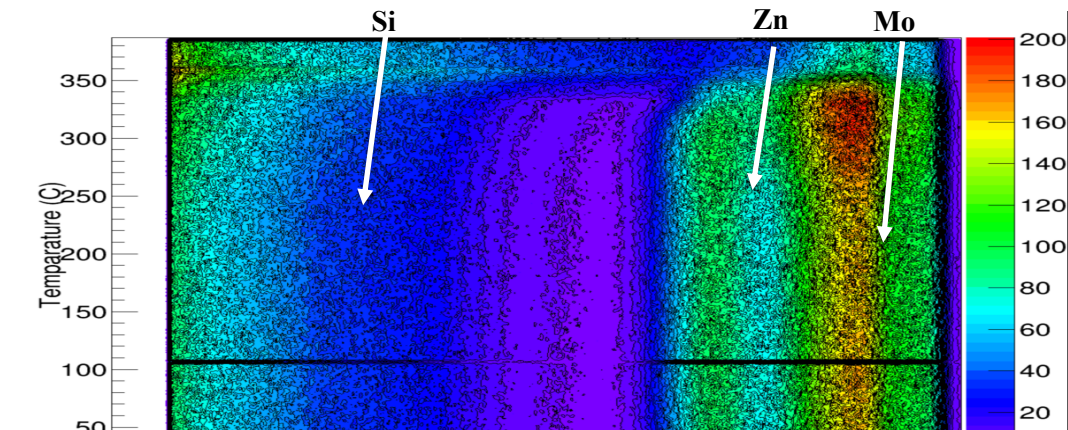
Fig. 4.13: *Contour plot representation obtained during real-time RBS analysis in 2-D from room temperature to 400 °C for silicon substrate.*

The contour plot provides clear view of the exact temperature where Zn atoms start diffusing through Mo and thus forming intermetallic Zn-Mo phase. From Fig. 4.13 the movement of atoms was noticeable at temperatures around 300 ℃ leading to very low Zn signals at temperature around 340 ℃.

Fig.4.14 shows schematic diagram of thickness of Zn atoms and Zn-Mo growing layer against the increasing temperature from room temperature to 400 ℃. There is a big decline in Zn signals which is evident in the figure below, leading to the growth in Zn-Mo growing layer thickness, showing that Zn atoms have diffused through Mo and mixed with Mo forming an alloy and some of the Zn evaporated at higher temperatures.

66
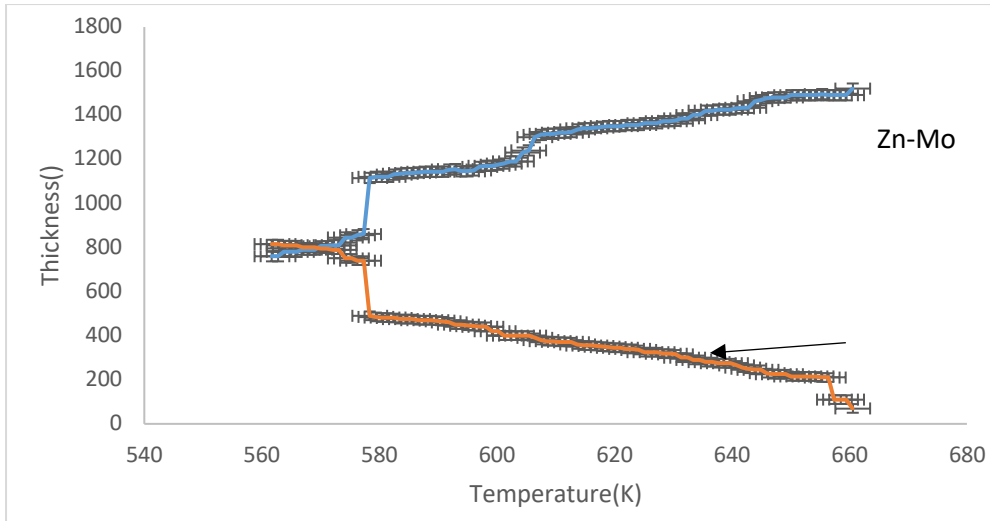
Fig. 4.14: *The graph of temperature against the thickness of the growing Zn-Mo layer and Zn layer from 300 ℃. The values are taken from SIMNRA software after simulation of the whole set of spectra from where the noticeable movements of atoms begin (around 300 ℃).*

The series of spectra from the temperature where the diffusion of Zn and Mo atoms at the inter-phase started to be observed from the spectra were selected, and simulated and analysed using SIMNRA software. The thickness of the layers and concentration of the constituent atoms recorded as the temperature increases, the activation energy calculations performed from the data (Thickness of layers and temperatures) recorded were used. In the schematic plots displayed in Fig. 4.15, from the data (thickness and temperature) acquired when simulating using SIMNRA software, the plots were constructed and activation energy determined from the slope.
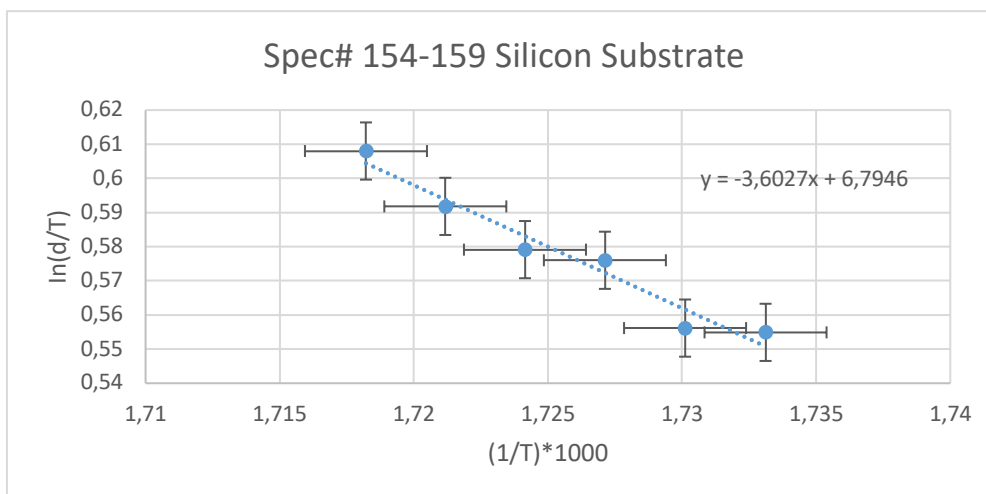
Fig. 4.15. *Plots showing data (temperature, composition and thickness) from SIMNRA software simulations and activation energy calculations from the slopes.*

The reaction dynamics which were monitored through real-time RBS showed that the atoms Zn and Mo atoms started reacting at the inter-phase at around 300 ℃ as reported, thus that's where the SIMNRA analyses was started and data extracted. With the monitoring program being set to count three spectra at a time with a rate of 3 ℃/min. From the plotted range of spectra in Fig. 4.15, the activation energy from the slope was estimated to be 0.31 eV (29.94 kJ/mole).

4.1.4. Surface Morphology and Microstructure of annealed Mo-Zn films

The annealed Mo-Zn films were further characterized for their surface morphology using FE-SEM and AFM, several temperatures (300 ℃, 340 ℃ and 360 ℃) of interest were chosen for the analysis. From the FE-SEM micrographs in Fig. 4.16, the surface morphology of the sample at 300 ℃ exhibited sphere like structures.

The observation of the surface morphology evolution can be explained based on the RBS simulation data, as shown in Table 4.1.
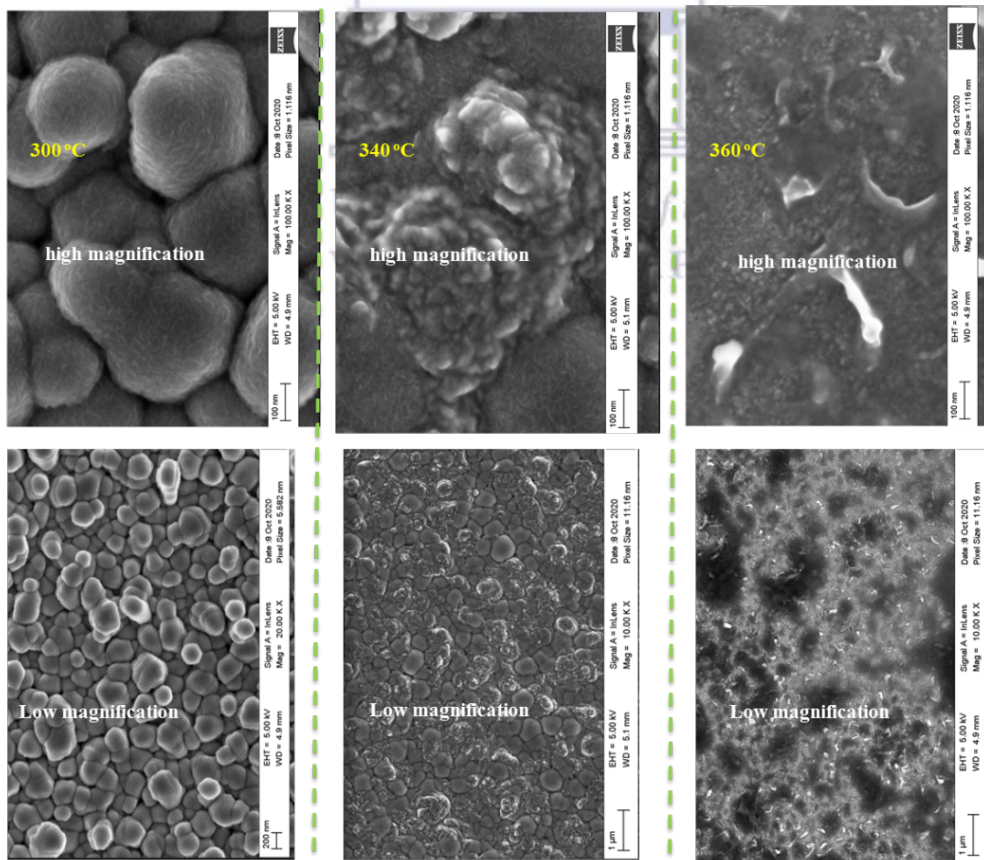
Fig. 4.16. *FE-SEM micrographs of annealed Mo-Zn film and temperatures of interest showing evolving surface morphology.*

68

Annealing Temperature	FE-SEM observation
300 ℃	1. Spherically shapes particles from Mo and Zn atoms bi-layer are observed. 2. At a higher magnification, there are ripples observed on the surface of the spheres that are due to Mo atoms which has crystallized from amorphous state seen in the as deposited film as seen from XRD pattern in Fig. 4.6.
340℃	1. The Zn start to diffuse and mix with Mo atoms at the inter-phase, as observed from texture change on the sample surface, and nucleation islands are seen on the film, and the film appearing to have cluster that are more densely packed. 2. At higher magnification, the Zn-Mo atoms exhibit granular conglomerate of the sample surface, this correlates to the RBS analysis, which showed Zn and Mo mixing.
360 ℃	1. Zn-Mo atoms has formed crystals of the sample surface, with the spherical shaped cluster merged into to semi-continuous film. 2. At higher magnification, there were no cluster observed as it was the case in 300 ℃ annealing, only dispersed crystals are observed.

Table 4.2: *Observation of the FE-SEM at various annealing temperatures.*

The FE-SEM cross section micrographs of the samples of the sample at temperature of interest are discussed in Table 4.2, based on the FE-SEM in Fig. 4.17.
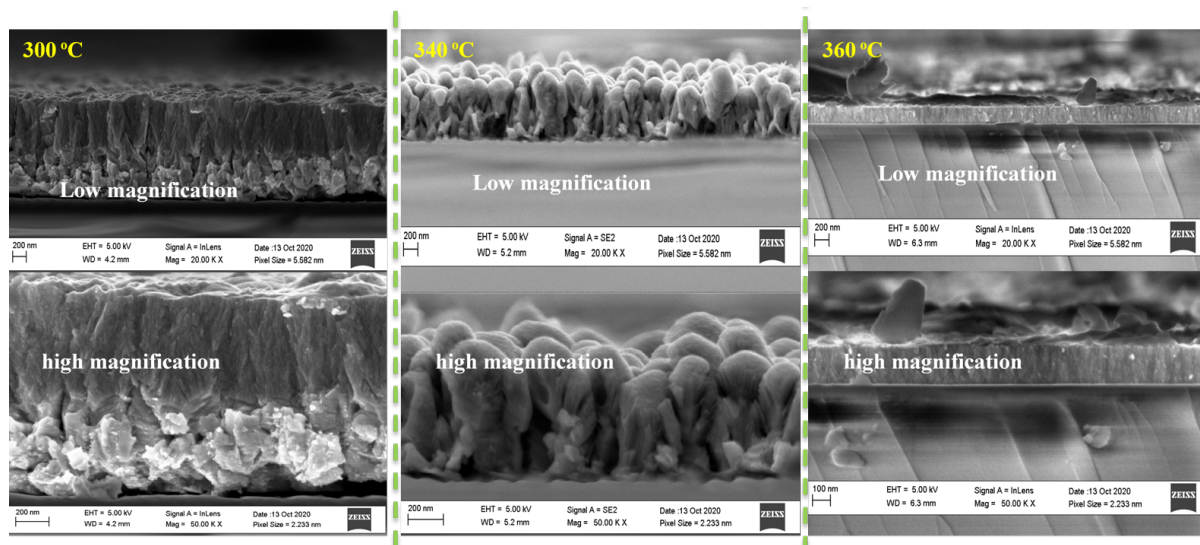
Fig. 4.17. *FE-SEM cross-section micrographs of annealed Mo-Zn film and temperatures of interest showing evolving surface morphology.*

Annealing Temperature	FE-SEM cross-section observation
300 ℃	1. At 300 ℃ the Mo and Zn atomic layers can be clearly distinguished, from their contrast which is based difference in atomic numbers, with darker layer being Mo and Zn a brighter region. 2. The diffusion of Zn starts at this temperature as noted from the brighter regions (*Zn atoms*) moving to the to the darker region *(Mo atoms*)
340 ℃	1. At this temperature Zn and Mo atoms have mixed forming a rough surface morphology with a cone like structures being observed. These cones like microstructure are Zn-Mo alloy based on the RBS data.
360 ℃	1. The surface morphology appear smoother, with the thickness of the film reduced, due evaporation of some of the Zn atom after diffusion. 2. The smoothness is as results of mixing of atoms resulting collapse of the cones structures observed at 340 ℃.

Table.4.3 Observation of the FE-SEM cross section of the sample at temperatures of interest.

Samples	Mean Area	Mean Length
As-deposited(small crystals)	19.125 nm	17.78nm
As-deposited(large crystals)	54.375 nm	53.29nm
Annealed at 300℃	38.2 µm	37.029 µm
Annealed 340℃(small)	31.286 nm	30.195 nm
Annealed 340℃(large)	56.429 nm	55.18 nm
Annealed 360℃	The surface morphology appear smoother resulting to no clear shaped particles to conduct measurements.	The surface morphology appear smoother resulting to no clear shaped particles to conduct measurements.

Table 4.4. *A table presenting the estimated mean area and length using ImageJ software of the identified particles for the samples, as-deposited, annealed at 300 ℃, 340 ℃ and 360 ℃.*

From ImageJ software particle analyses performed, samples exhibited variation in sizes of the visible and measurable particles, and their distribution. As-deposited sample for Zn-Mo system on glass substrate has the surface distributed particles of different sizes with a mean area ranging from 19.125 nm to 54.375 nm. When the sample annealed at 300 ℃ there is noticeable variation in sizes of the particles on the surface, with the mean area (recorded as 38.2 µm) and length (37.029 µm) showing an increase compared to un-annealed sample.

Nevertheless, when annealed at 340 ℃ the sizes of the surface crystals decreases and that's also evident on the estimated mean area ranging from 31.286 nm to 56.429 nm, and length from 30.195 nm to 55.18 nm. There was a complete mixing of surface particles at 360 ℃ annealing temperature leading to complications in measuring mean area and determining distribution of particles. SEM surface analyses contributed in the height examination of the deposited atoms, and Fig. 4.13 below displays cursor height results of the un-annealed sample.

4.1.4.1. Atomic Force Microscope (AFM) analyses

The AFM micrographs of the 300 ℃, 340 ℃ and 360 ℃ temperatures were plotted in 2-D and 3-D configuration as shown in Fig. 4.18.
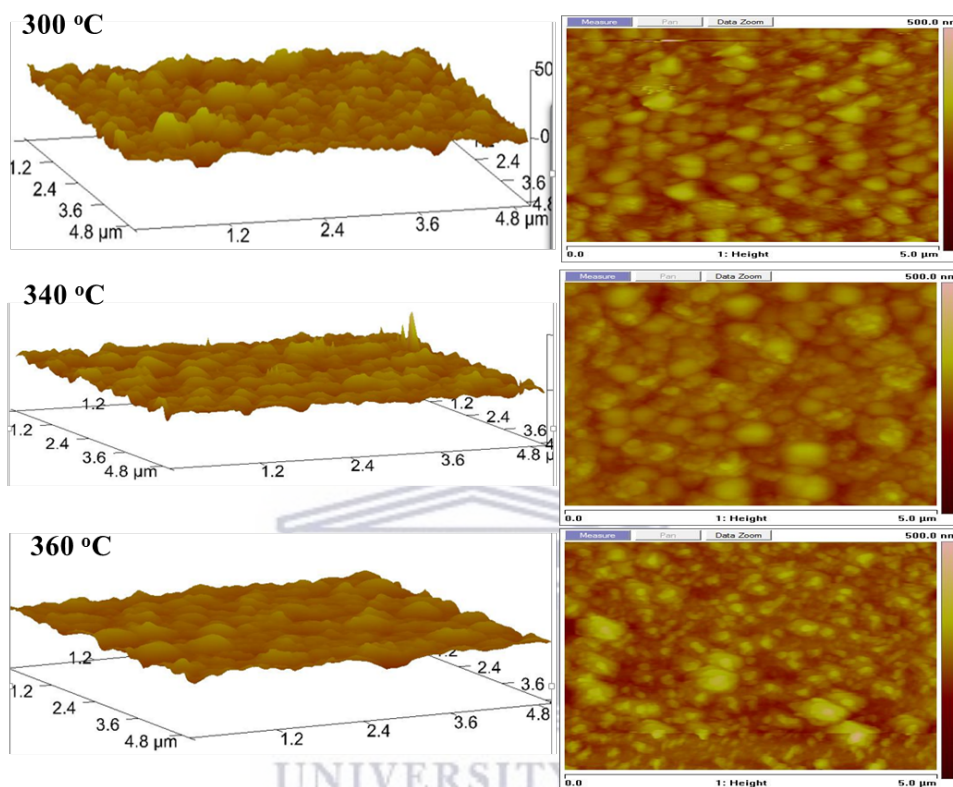
Fig.4.18. *2D and 3D AFM micrographs of Zn-Mo samples at temperatures 300 ℃, 340 ℃ and 360 ℃.*

From the AFM micrographs, the evolution of the sample surface roughness as the annealing temperature increases can be observed from Fig. 4.18, the root mean square roughness of the sample can be said to be reduced as the annealing temperature increases, even though this does not take place in a linear fashion as shown in

Annealing Temperature (℃)	Average Roughness (nm)
Un-annealed Zn/Mo	21.6 nm
Annealed Zn/Mo at 300 ℃	19.6 nm
Annealed Zn/Mo at 340 ℃	25.2 nm
Annealed Zn/Mo at 360 ℃	24.7 nm

Table .4.5. *Atomic force microscope sample roughness analysis.*

With the increase in temperature, the sizes of crystals on the surface tend to grow bigger, and consequently combine with other neighbouring crystals, this occurs by Zn and Mo atom forming nucleation sites, which then agglomerate and coalesce resulting in bigger crystal of mixed Zn and Mo atoms. As the temperature increases (*nucleation barrier is reduced*) [15], these islands combine to form the surface which become smoother with the increase in temperature. A higher nucleation density has been reported to be essential to form smoother films [44].

The variation on the annealing temperature influences the texture of the surface effectively, as it can improve the surface material for the desired properties [119].

4.1.4.2. X-ray diffraction analyses

Fig. 4.19 shows X-ray diffraction patterns of the Zn-Mo sample at 300 ℃, 340 ℃ and 360 ℃ annealing temperatures. The evolution of the microstructure of the film as observed from the diffraction patterns, shows that the Zn atoms migrate from the beneath the Mo layer to close to the surface, as seen from the increase in the intensity of the Zn Bragg peak at $2\theta = 36.4°$. At 300 ℃ there is an emergence of Zn-Mo diffraction pattern, this however does not appear that higher temperatures. This could suggest that at this temperature the Zn and Mo atoms start to mix and as the temperature increases, the Zn atoms migrate to near the surface of the sample.

The formation of Zn/Mo intermetallic phases on as-deposited sample was not visible from the XRD. The intensive Zn peak was noticeable at $2\theta = 36, 29°$, and weak diffraction peak of Mo observed at $2\theta = 40, 52°$ before annealing. The traces of Zn/Mo intermetallic phase was observed for sample annealed at 300 ℃ around $2\theta = 40, 91°$.
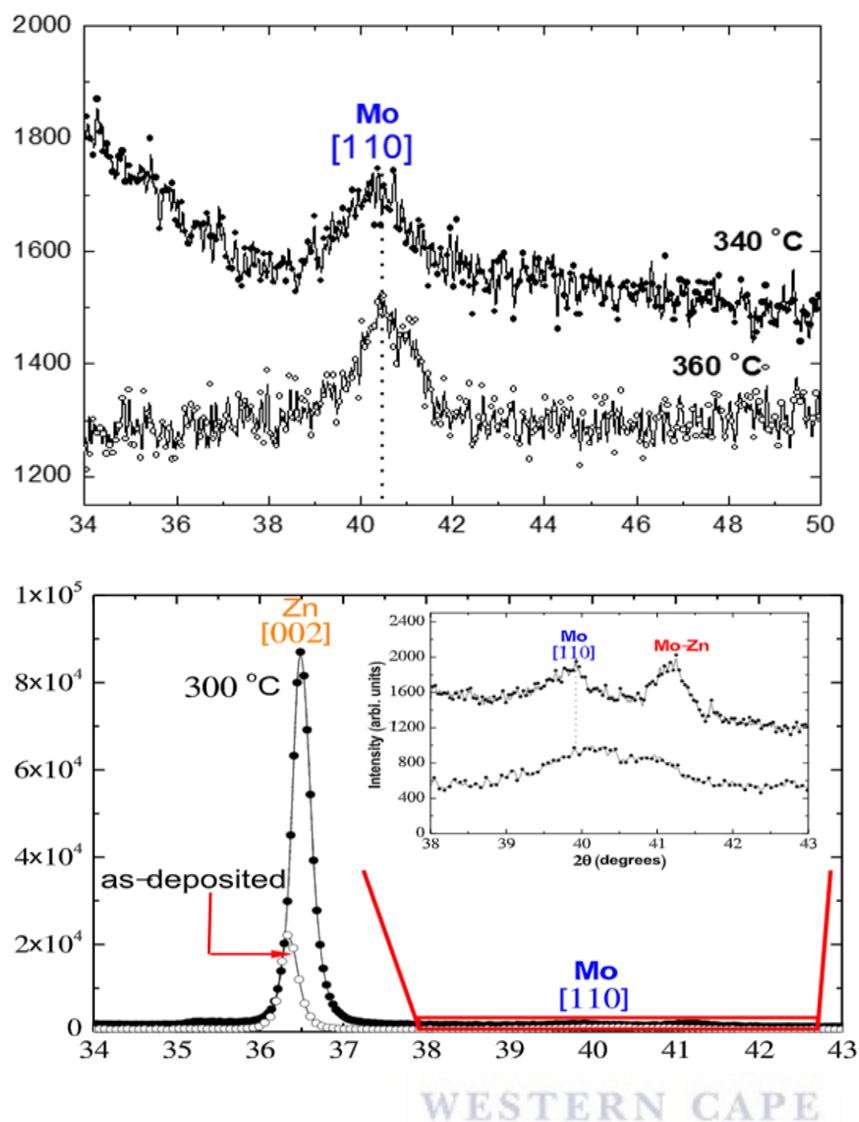
Fig. 4.19. *XRD results for samples prepared using electron beam evaporation system and further annealed using a furnace at different temperatures 300 ℃, 340 ℃ and 360 ℃.*

The entire pattern was analysed and searched for any available phases consists of Zn-Mo. The formation of Zn-Mo intermetallic phases on as-deposited sample was not visible from the XRD. The intensive Zn peak was noticeable at $2\theta = 36, 29°$, and weak diffraction peak of Mo observed at $2\theta = 40, 52°$ before annealing. The traces of Zn-Mo intermetallic phase was observed for sample annealed at 300 ℃ around $2\theta = 40, 91°$. The intensity of the Zn has increased when comparing un-annealed and annealed at 300 ℃ samples with the diffraction peak of Zn increases on those samples with the increase in temperature. The crystallite size of Zn and Mo phases from as-deposited to annealed samples are calculated using Scherrer equation (Eq. 6) and displayed in Table 4.6.

$$D = \frac{0,9\,\lambda}{\text{ß}\cos\theta}$$

(6)

Where, λ is the x-ray wavelength.

ß is the full width half maximum (FWHM)

θ is the Bragg angle

D is the crystallite size

Samples	λ (nm)	2θ (Rad)	ß	Size D (nm)	Material
As-deposited	1.540598	0,64	0,4	3,47	Zn
		0,71	1,5	0,92	Mo
Annealed (300 ℃)	1.540598	0,64	0,21	6,6	Zn
		0,70	0,9	1,54	Mo
		0,72	0,8	1,71	Zn-Mo
Annealed (340 ℃)	1.540598	0,71	1,1	1,26	Mo
Annealed (360 ℃)	1.540598	0,71	1,3	1,07	Mo

Table 4.6. *Results of the crystallite sizes on differently annealed samples, 300 ℃, 340 ℃ and 360 ℃ calculated using Scherrer equation.*

With intermetallic Zn-Mo phase only visible at temperature around 300 ℃, then at 340 ℃ Zn peak appeared to be diminishing. The intensities of Mo and Zn were varying with annealing temperature which that can indicate the movement of atoms from one layer to another, resulting in different stoichiometry. As the temperature increases, the intensity of Zn peaks drops. Annealing temperature has a major effect in the microstructure and the arrangement of atoms in the material, as it activates atoms thermally, resulting in a changed structure and properties [18].

4.2 Summary and results overview

Zn and Mo thin films on a glass and silicon substrate were successfully synthesized using electron beam evaporation system. Microstructure and Morphology of pristine Zn and Mo films were examined through SEM, AFM and XRD. Prepared Zn-Mo system was subjected to linear ramp from room temperature to 400 °C at a rate of 2 °C/min. At very lower temperatures below 100 °C there were no noticeable variation on the concentration of atoms of materials. However, as the temperature increased severely, Zn peak started dropping and that was noticeable at temperature around 300 °C for films deposited on silicon and 240 °C for films prepared on glass. With the Zn peak decreasing as the temperature increases, there was also a growing layer of Zn-Mo resulting from the diffusion of Zn atoms through Mo. It is also evident from SIMNRA simulations performed that the thickness of the layer having too much concentration of Zn drops, and the surface layer which had less concentration of Zn at lower temperatures, have grown up in thickness. For the films deposited on glass substrate, there were three peaks including the peak of Arsenic, which might be from elements making up glass. Even though there was a third peak between Zn and Mo, SIMNRA simulations proved that Zn concentration drops as the temperature increases, and this decline is because of Zn atoms diffusing through Mo, forming an alloy and some of Zn lost through evaporation. The collection of spectra from where the reaction starts for both substrates (silicon and glass) was analyzed with the thickness of the layers noted with respect to annealing temperature. Hence, activation energies were estimated for both substrates, with Zn-Mo bi-layer system on silicon having 0.31eV (29.94 kJ/mole), and on glass having 0.27eV (26.4 kJ/mole).

Bi-layer Zn-Mo films on glass were later subjected to vacuum annealing with the pressure 5×10^{-6} mbar, and their microstructure and morphologies studied. With the increase in annealing temperature, there is a remarkable growth in particles but subsequently decrease in size as the temperature neared 400 °C. AFM studies showed that there is a decrease in average roughness as the temperature increases, but that comparison can be made on films having the same thickness since the thickness of the grown thin films has an effect on the surface average roughness. The addition of Mo proved to have an impact on the microstructure of the films. XRD studies showed that there were no Zn-Mo intermetallic phases observable at lower temperatures, and was later observable at the annealing temperature around 300 °C.

CHAPTER 5

Conclusions and recommendations

5.1 Conclusions

The aim of the study was to prepare Zn-Mo thin films on glass substrate using electron beam evaporation system, compare and track diffusion kinetics using real-time RBS. The annealing was done isothermally (real-time RBS) where real-time RBS was used to track the diffusion kinetics in Zn-Mo metallic system from room temperature to 400 ℃.
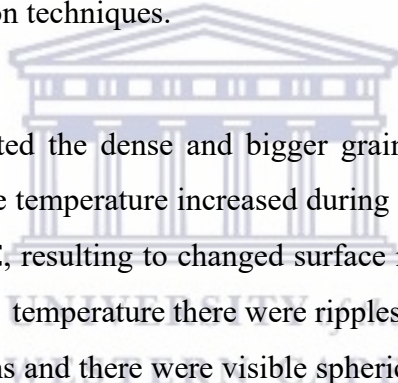
In this study the preparation of bi-layer thin films using e-beam system have been achieved, on a silicon substrate. Microstructure and morphology of un-annealed and annealed samples have been examined using XRD and SEM respectively. Zn-Mo thin films grown were annealed in in-situ real-time RBS and diffusion kinetics being tracked simultaneously during annealing. The surface roughness of the thin films before and after annealing were analysed through AFM.

Real-time RBS detailed a clear view on the formation of Zn-Mo phases and the temperature where the reaction begin and provides quantitative information throughout the reaction period. Annealing have the great effect on the morphology and microstructure of thin films, because of the growth it causes in the atoms of material, and thus leading to varying crystallite sizes and morphologies. This study aimed to compare and track diffusion kinetics using real-time RBS.

In-situ real-time RBS showed that the concentration of constituent atoms in Zn-Mo system depends on the temperature. At very lower temperature, there were no movements on the atoms of the whole system, and they were more noticeable as the temperature increased above 200 ℃. When the temperature reached 300 ℃, that's where the movement of Zn atoms was fully observable towards Mo and later evaporate as the temperature neared 400 ℃. SIMNRA simulations before and after real-time RBS showed that Zn has diffused through Mo, forming Zn-Mo phase and some Zn lost through evaporation. The movement of atoms was noticeable at temperatures around 300 ℃ leading to very low Zn signals at temperature around 340 ℃.

After full analysis from real-time RBS, samples were annealed in a vacuum using furnace at three temperatures and examined properties through AFM, SEM and XRD. Zn and Mo thin films on a silicon substrate were successfully synthesized using electron beam evaporation system.

Prepared Zn-Mo system was subjected to linear ramp from room temperature to 400 ℃ at a rate of 2 ℃/min. At very lower temperatures below 100 ℃ there were no noticeable variation on the concentration of atoms of materials as stated. With the Zn peak decreasing as the temperature increases, there was also a growing layer of Zn-Mo resulting from the diffusion of Zn atoms through Mo. It is also evident from SIMNRA simulations performed that the thickness of the layer having too much concentration of Zn drops, and the surface layer which had less concentration of Zn at lower temperatures, have grown up in thickness. The collection of spectra from where the reaction starts for silicon substrate was analyzed with the thickness of the layers noted with respect to annealing temperature. Bi-layer Zn-Mo films on glass were later subjected to vacuum annealing with the pressure 5×10^{-6} mbar, and their microstructure and morphologies studied. With the increase in annealing temperature, there is a remarkable growth in particles but subsequently decrease in size as the temperature neared 400 ℃. Zn-Mo bi-layer system before and after annealing as well as Zn film on silicon was characterised through different characterisation techniques.

SEM micrographs have exhibited the dense and bigger grains coalesces uniformly, which become bigger and bigger as the temperature increased during annealing. The grains combine at high temperature near 400 ℃, resulting to changed surface morphology and particle sizes. At high magnification in 300 ℃ temperature there were ripples observed on the surface of the spheres that are due to Mo atoms and there were visible spherically shaped particles from Mo and Zn atoms. The Zn and Mo atoms started to mix and the film appeared to have cluster that are more densely packed at 340 ℃. Zn-Mo atoms has formed crystals of the sample surface, with the spherical shaped cluster merged into to semi-continuous film at 360 ℃.

XRD data showed no visible Zn-Mo phase before annealing, and later observable after annealing at 300℃. The intensity of the Zn has increased when comparing un-annealed and annealed at 300 ℃ samples with the diffraction peak of Zn increased on those samples with the increase in temperature. The evolution of the microstructure of the film as observed from the diffraction patterns, showed that the Zn atoms migrated from the beneath the Mo layer to close to the surface. At 300 ℃ Zn-Mo diffraction pattern emerged, this however did not appear at higher temperatures. This could suggest that at this temperature the Zn and Mo atoms started to mix and as the temperature increases, the Zn atoms migrated to near the surface of the sample. As the temperature increased, the intensity of Zn peaks dropped. Annealing temperature has a major effect in the microstructure and the arrangement of atoms in the

78

material, as it activates atoms thermally, resulting in a changed structure and properties. The addition of Mo proved to have an impact on the microstructure of the films. XRD studies showed that there were no Zn-Mo intermetallic phases observable at lower temperatures, and was later observable at the annealing temperature around 300 ℃.

AFM studies showed that there is a decrease in average roughness as the temperature increases, but that comparison can be made on films having the same thickness since the thickness of the grown thin films has an effect on the surface average roughness. The average surface roughness of the bi-layer Zn-Mo system before annealed was studied and from the AFM micrographs, the evolution of the sample surface roughness as the annealing temperature increased the root mean square roughness of the sample can be said to be reduced as the annealing temperature increased. It showed that the surface is rough at low temperature compare to high. However, the thickness of films also proved to have significant impact on the surface average roughness. The samples synthesized with bigger thickness exhibited the surface with less average roughness. As the temperature increased the crystals of the mixed Zn and Mo atoms got bigger.

In conclusion, from this work it was investigated and proved that annealing temperature in real-time RBS has major influence on the surface and stoichiometry of the samples. It was evident from the analysis that as the temperature of annealing increased there was a severe movement on the atoms of the target material, and thus changing properties. The morphology of the surface of the sample depends on the annealing temperature, since it was proven that as the temperature increased, the surface becomes smooth. The study proved that the substrate, thickness, annealing have huge impact on the reaction dynamics on bi-layer thin metallic films.

REFERENCES

[1] Oaring, M., 2001. Materials science of thin films. *Elsevier (Vol 2) ISBN: 9780080491783.*

[2]. Vessel, J.L., Kern, W. and Kern, W. 1991. Thin film processes. *Elsevier (Vol. 2) ISBN: 9780323138987.*

[3]. Ranted, N.K., Mulan, S. and Widhiyanti, T., 2019. An analyses of multiple representation about intermolecular forces. *Journal of Physics: Conference Series, 1157, pp. 042029.*

[4].Hirschfeld, J.O., 2009. Intermolecular forces. *John Wiley & Sons (Vol. 24). ISBN: 0470143975, 9780470143971.*

[5]. Pullman, A., 2013. Intermolecular forces. *Springer Science & Business Media (Vol. 14). ISBN: 978-94-015-7658-1.*

[6]. Poling, B.E., Prausnitz, J.M. and O'Connell, J.P., 2001. Properties of gases and liquids. *McGraw-Hill Education. ISBN: 9780070116825.*

[7]. Levy, D.H., 2007. Van der Waals molecules. Advances in Chemical Physics. *John Wiley & Sons, ISBN: 0470143134, 9780470143131.*

[8]. Wenzel, C., Wetzig, K., Thomas, J., Hecker, M. and Bruckner, W., 2003. Thin film preparation and characterization technique. *Metal Based Thin Films for Electronics*, *https://doi.org/10.1002/3527602534.ch3.*

[9]. Kosugi, D., Hagio, T., Kamimoto, Y. and Ichino, R., 2017. Effect of the addition of molybdenum on the structure and corrosion resistance of zinc–iron plating. *Coatings, 7(12), p.235.*

[10]. Horváth, E., Németh, A., Koós, A.A., Bein, M.C., Tóth, A.L., Horváth, Z.E., Biró, L.P. and Gyulai, J., 2007. Focused ion beam based sputtering yield measurements on ZnO and Mo thin films. *Superlattices and Microstructures*, *42(1-6), p.392-397.*

[11]. Abegunde, O.O., Akinlabi, E.T., Oladijo, O.P., Akinlabi, S. and Ude, A.U., 2019. Overview of thin film deposition techniques. *AIMS Materials Science, 6(2), p.174.*

[12]. Świątek, Z., Kazimierczak, H., Ozga, P., Bonchyk, O. and Savytskyy, H., 2017. Structural and microstructural analysis of Zn–Mo alloy layers electrodeposited from aqueous citrate solution. *Metallofiz. Noveishie Tekhnol. 39(11), p.1547-1556.*

[13]. Islam, K. and Sharif, A., 2019. Characterization of Zn–Mo and Zn–Cr Pb-free composite solders as a potential replacement for Pb-containing solders. *Harsh Environment Electronics: Interconnect Materials and Performance Assessment. ISBN: 9783527344192.*

[14]. Pola, A., Tocci, M. and Goodwin, F.E., 2020. Review of microstructures and properties of zinc alloys. *Metals*, *10(2), p.253.*

[15]. Zhang, Z. and Lagally, M.G., 1997. Atomistic processes in the early stages of thin-film growth. *Science*, *276(5311), p.377-383.*

[16]. Gilmer, G.H. and Grabow, M.H., 1987. Models of thin film growth modes. *JOM, 39(6), p.19-23.*

[17]. Itagaki, N., Nakamura, Y., Narishige, R., Takeda, K., Kamataki, K., Koga, K., Hori, M. and Shiratani, M., 2020. Growth of single crystalline films on lattice-mismatched substrates through 3D to 2D mode transition. *Scientific reports, 10(1), p.1-10.*

[18]. Brune, H., 2014. Epitaxial growth of thin films. *Surface and Interface Science, 4, p.421-477.*

[19]. Schuck, C.F., Roy, S.K., Garrett, T., Yuan, Q., Wang, Y., Cabrera, C.I., Grossklaus, K.A., Vandervelde, T.E., Liang, B. and Simmonds, P.J., 2019. Anomalous Stranski-Krastanov growth of (111)-oriented quantum dots with tunable wetting layer thickness. *Scientific reports, 9(1), p.1-10.*

[20]. Baylan, S., 2017. Diffusion assisted synthesis of metal nanotubes. *Thesis: elib.uni-stuttgart.de, p.1-32*

[21]. Kamiya, I. and Roca, R.C.I., 2021. Submonolayer stacking growth of In (Ga)/As nanostructures for opto-electronic applications: an alternative for Stranski-Krastanov growth. *Japanese Journal of Applied Physics, 60, p.1-9.*

[22]. Heo, H., Sung, J.H., Ahn, J.H., Ghahari, F., Taniguchi, T., Watanabe, K., Kim, P. and Jo, M.H., 2017. Frank–van der Merwe Growth versus Volmer–Weber Growth in successive stacking of a few-layer Bi2Te3/Sb2Te3 by van der Waals heteroepitaxy: *Advanced Electronic Materials, 3(2), p.1600375.*

[23]. Jachowicz, M., 2020. Properties of thin coatings deposited by physical vapour deposition on safety helmets. *International Journal of Occupational Safety and Ergonomics*, 27, *p.55-62.*

[24]. Baptista, A., Silva, F.J.G., Porteiro, J., Míguez, J.L., Pinto, G. and Fernandes, L., 2018. On the physical vapour deposition (PVD): evolution of magnetron sputtering processes for industrial applications. *Procedia Manufacturing, 17, p.746-757.*

[25]. Reichelt, K. and Jiang, X., 1990. The preparation of thin films by physical vapour deposition methods. *Thin Solid Films, 191(1), p.91-126.*

[26]. Mahan, J.E., 2000. Physical vapor deposition of thin films. *John Wiley & Sons. ISBN: 978-0471330011, p. 336.*

[27]. Reichelt, K. and Jiang, X., 1990. The preparation of thin films by physical vapour deposition methods. *Thin Solid Films, 191(1), p.91-126.*

[28]. Maiti, N., Karmakar, P., Barve, U.D. and Bapat, A.V., 2008. An evaporation system for film deposition using electron beam sources. *Journal of Physics: Conference Series, 114, p. 012049.*

[29]. Wang, Z. and Zhang, Z., 2016. Electron beam evaporation deposition. *Advanced Nano Deposition Methods, p.33-58.*

[30]. Shi, F., 2018. Introductory chapter: basic theory of magnetron sputtering. *Magnetron sputtering Intechopen, p.1-3.*

[31]. Valbusa, U., Boragno, C. and De Mongeot, F.B., 2002. Nanostructuring surfaces by ion sputtering. *Journal of Physics: Condensed Matter, 14(35), p.8153.*

[32]. Swann, S., 1988. Magnetron sputtering. *Physics in technology, 19(2), p.67.*

[33]. Morosanu, C.E., 2016. Thin films by chemical vapour deposition. *Elsevier (Vol 2) ISBN: 978-0-444-98801-0.*

[34]. Jones, A.C. and Hitchman, M.L., 2009. Overview of chemical vapour deposition. *Chemical Vapour Deposition: Precursors, Processes and Applications, 1, p.1-36.*

[35]. Sun, L., Yuan, G., Gao, L., Yang, J., Chhowalla, M., Gharahcheshmeh, M.H., Gleason, K.K., Choi, Y.S., Hong, B.H. and Liu, Z., 2021. Chemical vapour deposition. *Nature Reviews Methods Primers, 1(1), p.1-20.*

[36]. Oura, K., Lifshits, V.G., Saranin, A.A., Zotov, A.V. and Katayama, M., 2013. Surface science: an introduction. *Springer Science & Business Media ISBN: 9783662051795.*

[37]. Park, S.I., Quan, Y.J., Kim, S.H., Kim, H., Kim, S., Chun, D.M., Lee, C.S., Taya, M., Chu, W.S. and Ahn, S.H., 2016. A review on fabrication processes for electrochromic devices. *International Journal of Precision Engineering and Manufacturing-Green Technology, 3(4), pp.397-421.*

[38]. Ahmadi, S., Asim, N., Alghoul, M.A., Hammadi, F.Y., Saeedfar, K., Ludin, N.A., Zaidi, S.H. and Sopian, K., 2014. The role of physical techniques on the preparation of photoanodes for dye sensitized solar cells. *International Journal of Photoenergy, p.1-19.*

[39]. Hughes, M., 2016. What is Pulsed DC Sputtering. *URL: http://www. semicore. com/news/95-what-is-pulsed-dc-sputtering (accessed: 22.09. 2020).*

[40]. Kern, W., 2012. Thin film processes II. *Elsevier (Vol. 2) ISBN: 0080524214, 9780080524214.*

[41]. Magnfält, D., 2014. Fundamental processes in thin film growth: The origin of compressive stress and the dynamics of the early growth stages. *Doctoral dissertation, Linköping University Electronic Press.*

[42]. Manning, T. D., Parkin, I. P., Clark, R. J., Sheel, D., Pemble, M. E., & Vernadou, D. (2002). Intelligent window coatings: atmospheric pressure chemical vapour deposition of vanadium oxides. *Journal of Materials Chemistry, 12(10), p.2936-2939.*

[43]. Santos, H.S., Correa, A.A., Gromboni, M.F. and Mascaro, L.H., 2019. Electrodeposition study of the Cu-Zn-Mo system in citrate/sulfate medium. *Eclética Química Journal, p.26-35.*

[44]. Zhang, G., Yu, S., Yang, Y., Jiang, W., Zhang, S. and Huang, B., 2010. Synthesis, morphology and phase transition of the zinc molybdates ZnMoO4· 0.8 H2O/α-ZnMoO4/ZnMoO4 by hydrothermal method. *Journal of crystal growth, 312(11), p.1866-1874.*

[45]. Swapna, R. and Kumar, M.S., 2012. The role of substrate temperature on the properties of nanocrystalline Mo doped ZnO thin films by spray pyrolysis. *Ceramic International, 38(5), p.3875-3883.*

[46]. Liu, H., 2020. Growth kinetics of thin film epitaxy. *Century Surface Science-a Handbook. DOI: 10.5772/intechopen.91224*

[47]. Kazimierczak, H., Ozga, P., Świątek, Z. and Bielańska, E., 2013. Characterisation of Zn–Mo alloy layers electrodeposited from aqueous citrate solution. *Journal of alloys and compounds, 578, p.82-89.*

[48]. Hara, A., Świątek, Z. and Ozga, P., 2020. The role of surfactants in induced electrodeposition of Zn–Mo layer from citrate solutions. *Journal of Alloys and Compounds, 827, p.154195.*

[49]. Kazimierczak, H., Morgiel, J., Swiatek, Z., Vega, J.M. and García-Lecina, E., 2018. Effect of Mo addition on corrosion of Zn coatings electrodeposited on steel. *Corrosion Science, 135, p.107-119.*

[50]. Ahmed, M.Z. and Bhattacharjee, P.P., 2014. Evolution of microstructure and texture during isothermal annealing of a heavily warm-rolled duplex steel. *Isij International, 54(12), p.2844-2853.*

[51]. Khodabakhshi, A.R. and Kazeminezhad, M., 2019. Effects of non-isothermal annealing on microstructure and mechanical properties of severely deformed aluminum samples: Modeling and experiment. *Transactions of Nonferrous Metals Society of China, 29(6), p.1127-1137.*

[52]. Wang, S.F., Yang, H.C., Liu, C.F. and Bor, H.Y.Y., 2014. Characteristics of bilayer molybdenum films deposited using RF sputtering for back contact of thin film solar cells. *Advances in Materials Science and Engineering, p.1-6.*

[53]. Mostako, A.T.T. and Rao, C.V.S., 2010, February. Pulsed laser deposition of thin film of molybdenum. In *Journal of Physics: Conference Series*, 208, p. 012114.

[54]. Li, J. and Sun, J., 2017. Application of X-ray diffraction and electron crystallography for solving complex structure problems. *Accounts of chemical research, 50(11), p.2737-2745.*

[55]. Kim, S., Kim, K.S., Izuta, G. and Suganuma, K., 2008, September. Reliability of die attached AlN-DBC module using Zn-Sn high temperature lead-free solders. *2ⁿᵈ Electronics System-Integration Technology Conference, p. 411-416.*

[56]. Díaz-Morales, O., Mostany, J., Borrás, C. and Scharifker, B.R., 2013. *Journal of Solid State Electrochemistry 17, p.45–351.*

[57]. Agapie, M., Peter, I. and Varga, B., 2015. Structure of cooled Zn-Al eutectoid based alloys in biphasic domain. J*ournal of Optoelectronics and Advanced Materials*, 17, p.1842-1848.

[58]. Mallick, S., Kabir, M.S. and Sharif, A., 2016. Study on the properties of Zn–xNi high temperature solder alloys. *Journal of Materials Science: Materials in Electronics, 27,4,, p.3608-3618.*

[59]. Theron, C.C., Lombaard, J.C. and Pretorius, R., 2000. Real-time RBS of solid-state reaction in thin films. *Nuclear Instruments and Methods in Physics Research Section B: Beam Interactions with Materials and Atoms, 161, p.48-55.*

[60]. Theron, C.C., Mars, J.A., Churms, C.L., Farmer, J. and Pretorius, R., 1998. In situ, real-time RBS measurement of solid state reaction in thin films. *Nuclear Instruments and Methods in Physics Research Section B, 139(1-4), p.213-218.*

[61]. Roszkowska, A.M., Urso, M., Signorino, A. and Aragona, P., 2018. Use of the femtosecond lasers in ophthalmology. *EPJ Web of Conferences, 167, p. 05004.*

[62]. Callou, T.P., Garcia, R., Mukai, A., Giacomin, N.T., de Souza, R.G. and Bechara, S.J., 2016. Advances in femtosecond laser technology. *Clinical Ophthalmology*, *10, p.697.*

[63]. Tong, X.L., Jiang, D.S., Liu, L., Liu, Z.M. and Luo, M.Z., 2007. Effect of the laser fluence on structural and optical characterization of thin CdS films synthesized by femtosecond pulsed laser deposition. *Optics communications, 270(2), p.356-360.*

[64]. Zhu, Q. and Shen, M., 2015. Femtosecond laser irradiation-induced infrared absorption on silicon surfaces. *International Journal of Smart and Nano Materials*, *6(2), p.113-123.*

[65]. Shao-Xu, H., Pei-De, H., Li-Peng, G., Xue, M., Xin-Yi, L. and Yu-Jie, F., 2012. The effects of femtosecond laser irradiation and thermal annealing on the optoelectronic properties of silicon supersaturated with sulfur. *Chinese Physics Letters, 29(4), p.046101.*

[66]. Cik, R.C.H., Foo, C.T. and Nor, A.F.O., 2015. Field emission scanning electron microscope facility in BTI. *Nuclear Technical Convention, Malaysia, p.1-6.*

[67]. Liu, D., Yang, Z., Wang, Z. and Zhang, C., 2010. Synthesis and evaluation of corrosion resistance of molybdate-based conversion coatings on electroplated zinc. *Surface and Coatings Technology, 205, p. 2328-2334.*

[68]. Po, R., Corso, G., Cominetti, A., Carbonera, C., Bernardi, A., Di Paola, E., Carati, C. and Bonoldi, L., 2019. Field emission scanning electron microscopy (FESEM): an easy way to characterize morphologies of P3HT: PCBM coated and printed solar cells. *Flexible and Printed Electronics*, *4(3), p.034001.*

[69]. Alyamani, A.M.O.L. and Lemine, O.M., 2012. FE-SEM characterization of some nanomaterial. *Scanning Electron Microscopy*. *DOI: 10.5772/34361, IntechOpen.*

[70]. Havrdova, M., Polakova, K., Skopalik, J., Vujtek, M., Mokdad, A., Homolkova, M., Tucek, J., Nebesarova, J. and Zboril, R., 2014. Field emission scanning electron microscopy (FE-SEM) as an approach for nanoparticle detection inside cells. *Micron*, *67, p.149-154.*

[71]. Goldstein, J.I., Newbury, D.E., Michael, J.R., Ritchie, N.W., Scott, J.H.J. and Joy, D.C., 2017. Scanning electron microscopy and X-ray microanalysis. *Springer Science & Business Media, ISBN: 978-1-4615-0215-9.*

[72]. Ameh, E.S., 2019. A review of basic crystallography and x-ray diffraction applications. *The International Journal of Advanced Manufacturing Technology*, *105(7), p.3289-3302.*

[73]. Zolotoyabko, E., 2014. Basic concepts of X-ray diffraction. *John Wiley & Sons, ISBN: 3527335617, 9783527335619.*

[74]. Bunaciu, A.A., UdriȘTioiu, E.G. and Aboul-Enein, H.Y., 2015. X-ray diffraction: instrumentation and applications. *Critical Reviews In Analytical Chemistry, 45(4), p.289-299.*

[75]. Warren, B.E., 1990. X-ray Diffraction. *Courier Corporation, ISBN: 0486141616, 9780486141619.*

[76]. Perutz, M.F., 1990. How WL Bragg invented X-ray analysis. *Acta Crystallographica Section A: Foundations of Crystallography*, *46*(8*), p.633-643.*

[77]. Bragg, W.L., 1914. The analysis of crystals by the X-ray spectrometer. *Proceedings of the Royal Society of London. Series A, Containing Papers of a Mathematical and Physical Character*, *89*(613*), p.468-489.*

[78]. Smith, F., 1999. Industrial applications of X-ray diffraction. *CRC press, ISBN: 9780824719920.*

[79]. Thibault, P. and Elser, V., 2010. X-ray diffraction microscopy. *The Annual Review of Condensed Matter Physics., 1(1), p.237-255.*

[80]. Jauncey, G.E.M., 1924. The scattering of x-rays and Bragg's law. *Proceedings of the National Academy of Sciences of the United States of America*, *10(2), p.57.*

[81]. Mayer, M., 2003. Rutherford backscattering spectrometry (RBS). *Workshop on Nuclear Data for Science and Technology: Materials Analysis (Vol. 34).*

[82]. Kötz, R., Gobrecht, J., Stucki, S. and Pixley, R., 1986. In situ rutherford backscattering spectroscopy for electrochemical interphase analysis. *Electrochimica acta, 31(2), p.169-172.*

[83]. Perrière, J., 1987. Rutherford backscattering spectrometry. *Vacuum*, *37(5-6), p.429-432.*

[84]. Jeynes, C., Barradas, N.P. and Szilágyi, E., 2012. Accurate determination of quantity of material in thin films by Rutherford backscattering spectrometry. *Analytical Chemistry, 84 (14), p. 6061-6069.*

[85]. Brocklebank, M., Noël, J.J. and Goncharova, L.V., 2019. In Situ Rutherford Backscattering Spectrometry for Electrochemical Studies. *Journal of The Electrochemical Society, 166(11), p. C3290.*

[86]. Chu, W.K. and Liu J.R, 1996. Rutherford backscattering spectrometry: reminiscences and progresses. *Materials Chemistry and Physics, (36), p. 183-188.*

[87]. Mora, C.M., 2018. Characterizing scattering cross-sections and stopping power of ionizing radiation in matter. *McNair Scholars Research Journal, 5(1), p.2.*

[88]. Perrière, J., 1987. Rutherford backscattering spectrometry. *Vacuum*, *37(5-6), p.429-432.*

[89]. Krieg, M., Fläschner, G., Alsteens, D., Gaub, B.M., Roos, W.H., Wuite, G.J., Gaub, H.E., Gerber, C., Dufrêne, Y.F. and Müller, D.J., 2019. Atomic force microscopy-based mechanobiology. *Nature Reviews Physics, 1(1), p.41-57.*

[90]. Korolkov, V.V., Summerfield, A., Murphy, A., Amabilino, D.B., Watanabe, K., Taniguchi, T. and Beton, P.H., 2019. Ultra-high resolution imaging of thin films and single strands of polythiophene using atomic force microscopy. *Nature communications*, *10*(1), p.1-8.

[91]. Crozier, K.B., Yaralioglu, G.G., Degertekin, F.L., Adams, J.D., Minne, S.C. and Quate, C.F., 2000. Thin film characterization by atomic force microscopy at ultrasonic frequencies. *Applied physics letters*, *76(14), p.1950-1952.*

[92] Eaton, P. and West, P., 2014. Atomic force microscopy. *MRS Bulletin, 29 ISBN: 978-0-19-957045-4.*

[93]. Meyer, E., 1992. Atomic force microscopy. *Progress in surface science*, *41*(1*), p.3-49.*

[94]. Blanchard, C.R., 1996. Atomic force microscopy. *The chemical educator, 1(5), p.1-8.*

[95] Neimash, V., Shepelyavyi, P., Dovbeshko, G., Goushcha, A.O., Isaiev, M., Melnyk, V., Didukh, O. and Kuzmich, A., 2016. Nanocrystals growth control during laser annealing of Sn:(α-Si) composites. *Journal of Nanomaterials, p. 1-7.*

[96]. Shewmon, P., 2016. Diffusion in solids. *Springer Science & Business Media, ISBN: 978-3-319-48206-4.*

[97]. Mehrer, H., 2007. Diffusion in solids: fundamentals, methods, materials, diffusion-controlled processes. *Springer Science & Business Media, (Vol. 155), ISBN: 978-3-540-71488-0.*

[98]. Elcock, E.W. and McCombie, C.W., 1958. Vacancy diffusion in binary ordered alloys. *Physical Review, 109(2), p.605.*

[99]. Barrer, R.M. and Jost, W., 1949. A note on interstitial diffusion. *Transactions of the Faraday Society, 45, p.928-930.*

[100]. Vasudevan, M. and Palanichamy, P., 2002. Characterization of microstructural changes during annealing of cold worked austenitic stainless steel using ultrasonic velocity measurements and correlation with mechanical properties. *Journal of materials engineering and performance*, *11(2), p.169-179*.

[101]. Chen, J., Shan, J.Y., Tsukada, T., Munekane, F., Kuno, A., Matsuo, M., Hayashi, T., Kim, Y.A. and Endo, M., 2007. The structural evolution of thin multi-walled carbon nanotubes during isothermal annealing. *Carbon, 45(2), p.274-280.*

[102]. Rath, B.B., 1995. Kinetics of nucleation and growth processes. *Materials Science and Engineering: B*, *32(3), p.101-106.*

[103]. Shiau, L.D., 2018. Determination of the Nucleation and Growth Kinetics for Aqueous L-glycine Solutions from the Turbidity Induction Time Data. *Crystals*, *8*(11)*, p.403.*

[104]. Baker, L.E., Pierce, A.C. and Luks, K.D., 1982. Gibbs energy analysis of phase equilibria. *Society of Petroleum Engineers Journal*, *22(05), p.731-742*.

[105]. Kashchiev, D., 2000. Nucleation: Basic theory with applications. *Elsevier, ISBN: 978-0-7506-4682-6.*

[106] Brewer, L. and Lamoreaux, R., 1980. The Lr-Mo system (Lawrencium-Molybdenum)*. Bulletin of Alloy Phase Diagrams, 1, p.81-82.*

[107]. Wichterle, I., Linek, J., Wagner, Z. and Fontaine, J., Sosnkowska-Kehiaian, K. and Kehiaian, H.V., 2008. Landolt-Bornstein. New Series Group IV: Physical Chemistry. *Springer*, *ISBN: 3-540-28004-9.*

[108]. Olvera, J.N.R., Martínez, J.A., Hernández, H.H., Orozco, I.G. and Arceo, L.D.B., 2017. Microstructural characterization and thermodynamic analysis of MoZn produced by mechanical alloying. *Journal of Alloys and Compounds*, *696, p.329-337.*

[109]. Prach, M. and Koleňák. R., 2015. Soldering of copper with high-temperature Zn-based solders. *Procedia Engineering, 100, p.1370-1375.*

[110]. Borg, R.J. and Dienes, G.J., 2012. An introduction to solid state diffusion. *Elsevier, ISBN: 9780323138406.*

[111]. Eskil, A., Lindström, T., Käck, B., Malmberg, C. and Asp, A., 2017. Simulation of thin Aluminium-foil in the packaging industry. *AIP Conference Proceedings, 1896, p. 160014.*

[112]. Srivastava, S., Jain, S.K., Gupta, G., Senguttuvan, T.D. and Gupta, B.K., 2020. Boron-doped few-layer graphene nanosheet gas sensor for enhanced ammonia sensing at room temperature. *RSC Advances, 10(2), p.1007-1014.*

[113]. Khodair, Z.T., Alsrraf, A.R., Manssor, M.I. and Bakr, N.A., 2012. Synthesis and study of ZnO nanorods and Fe-doped ZnO nanoflowers by atmospheric pressure chemical vapor deposition (APCVD) technique. *Journal of Electron Devices, 15, p.1200-1208.*

[114] Mtshali, C., Khumalo, Z., Mocumi, G., Lebesana, K., Kheswa, N., Magogodi, S., Cummings, F., Pieters, C. and Nkosi, M., 2019. Effects of argon thermal annealing on surface structure, microstructural and silicide formation of Silicon-Titanium-Cobalt thin film. *Nuclear Instruments and Methods in Physics Research Section B*, *445, p.18-25.*

[115] Zhao, D., Sathasivam, S., Li, J. and Carmalt, C., 2020. Transparent and conductive Molybdenum-doped ZnO thin films via chemical vapor deposition. *ACS Applied Electronic Materials Forums, 2(1), p.120-125.*

[116] Radha, R., Sakthivelu, A., & Raj, P. (2016). Synthesis and characterization of Molybdenum doped ZnO thin films by SILAR deposition method. *IRA-International Journal of Applied Sciences, 4(1), p.2455-4499.*

[117] Elcock, E. W. and McCombie, C. W., 1958. Vacancy diffusion in binary ordered alloys. *Physical Review, 109(2), p.605*.

[118] Barrer, R. M. and Jost, W., 1949. A note on interstitial diffusion. *Transactions of the Faraday Society*, *45, p.928-930.*

[119] Husna, J., Aliyu, M. M., Islam, M. A., Chelvanathan, P., Hamzah, N. R., Hossain, M. S., Karim, M.R. and Amin, N., 2012. Influence of annealing temperature on the properties of ZnO thin films grown by sputtering. *Energy Procedia, 25, p.55-61.*

Appendix A

Rutherford backscattering spectrometry simulated plot of the Zn-Mo samples used to calculate activation energy

93